nature materials

Letter

https://doi.org/10.1038/s41563-025-02312-9

# Memsensing by surface ion migration within Debye length

Received: 16 May 2024

Accepted: 3 July 2025

Published online: 1 August 2025

Check for updates

Ruihan Guo[1,2], Qixin Feng[2,3], Ke Ma[1], Gi-Hyeok Lee[4], Moniruzzaman Jamal[1,2,5,6], Xiao Zhao[1,2], Karen C. Bustillo[5], Jiawei Wan[1,2], Duncan S. Ritchie[1], Linbo Shan[7], Yuhang Cai[1,2], Jiachen Li[1,2], Jack Shen[1], Kaichen Dong[8,9], Ru Huang[7,10], Yimao Cai[7,10], Feng Wang[2,3], Miquel Salmeron[1,2], Haimei Zheng[1,2], Matthew Sherburne[1], Mary Scott[1,2,5], Wanli Yang[4], Mark Asta[1,2], Kechao Tang[7,10] ✉ & Junqiao Wu[1,2] ✉

Integration between electronics and biology is often facilitated by iontronics, where ion migration in aqueous media governs sensing and memory. However, the Debye screening effect limits electric fields to the Debye length, the distance over which mobile ions screen electrostatic interactions, necessitating external voltages that constrain the operation speed and device design. Here we report a high-speed in-memory sensor based on vanadium dioxide ($VO_2$) that operates without an external voltage by leveraging built-in electric fields within the Debye length. When $VO_2$ contacts a low-work-function metal (for example, indium) in a salt solution, electrochemical reactions generate indium ions that migrate into the $VO_2$ surface under the native electric field, inducing a surface insulator-to-metal phase transition of $VO_2$. The $VO_2$ conductance increase rate reflects the salt concentration, enabling in-memory sensing, or memsensing of the solution. The memsensor mimics *Caenorhabditis elegans* chemosensory plasticity to guide a miniature boat for adaptive chemotaxis, illustrating low-power aquatic neurorobotics with fewer memory units.

Understanding and simulating neural information processing is essential for neuromorphic computing[1,2], artificial sensing systems[3] and bioinspired robotics[4,5]. Cellular environments are inherently aqueous, where neural signals are transmitted by the transport of ions ($Na^+$, $K^+$, $Ca^{2+}$ and so on)[6]. Iontronics, which enable diverse electronic functions by manipulating ion movement in aqueous solutions, serve as a critical bridge between solid-state electronics and biological systems[7,8]. In iontronics, ion motion leads to both responsive adjustments to external stimuli for sensing and localized accumulation with high degeneracy for memory[7]. These functions allow iontronics to effectively mimic the dynamic and adaptive nature of biological responses. However, the Debye screening effect of mobile ions in an aqueous environment impedes interionic interactions beyond the screening length, imposing a challenge in the development of long-range sensory and memory functions. Current solutions include three-terminal transistors with liquid-gated voltages such as organic electrochemical transistors[9–11] and two-terminal memristors with confined nanoscale channels[2,12,13]. These methods require control via external voltage bias in aqueous

[1]Department of Materials Science and Engineering, University of California, Berkeley, CA, USA. [2]Materials Sciences Division, Lawrence Berkeley National Laboratory, Berkeley, CA, USA. [3]Physics Department, University of California, Berkeley, CA, USA. [4]Advanced Light Source, Lawrence Berkeley National Laboratory, Berkeley, CA, USA. [5]National Center for Electron Microscopy, Molecular Foundry, Lawrence Berkeley National Laboratory, Berkeley, CA, USA. [6]Materials and Metallurgical Engineering, Bangladesh University of Engineering and Technology, Dhaka, Bangladesh. [7]School of Integrated Circuits, Peking University, Beijing, China. [8]Institute of Data and Information, Tsinghua Shenzhen International Graduate School, Tsinghua University, Shenzhen, China. [9]Center of Double Helix, Tsinghua Shenzhen International Graduate School, Tsinghua University, Shenzhen, China. [10]Beijing Advanced Innovation Center for Integrated Circuits, Beijing, China. ✉e-mail: tkch@pku.edu.cn; wuj@berkeley.edu

environments, which complicates design and nanofabrication, highlighting the need for autonomous material platforms for memory and sensing at a simpler, more fundamental level.

Recent works have featured the use of non-volatile phase transition in bioinspired information processing[14,15]. Vanadium dioxide ($VO_2$), a correlated electron material recognized for its phase transition from insulator to metal near 67 °C, has emerged as an important material platform[16]. Researchers have stabilized the metallic phase of $VO_2$ at room temperature using gate voltages across ionic liquids[17,18]. By either introducing ion dopants or creating oxygen vacancies, this method incrementally modulates the conductance of $VO_2$ in response to gate-voltage changes. However, although the voltage-driven phase transition shows potential for in-memory computing, the approach is not suitable for sensing in aqueous environments[19]. Moreover, the sluggish nature of ionic motion in ionic liquids compromises the inherently fast phase transition in $VO_2$.

## Memsensor without external voltage

Here we introduce an in-memory sensor using the surface phase transition of $VO_2$ in aqueous solutions without the need for external voltages. This device exemplifies a memsensor[20], a concept to describe two-terminal devices exhibiting memristive behaviour and adaptability to changes in non-electrical external stimuli. Our memsensor comprises a $VO_2$ film (Supplementary Fig. 1) in direct contact with indium metal. When simply immersed in a NaCl solution, mobile indium ions are produced within a distance shorter than the Debye length from the oxide surface through electrochemical reactions. These ions are driven into the $VO_2$ film by the built-in electric fields at the solid–liquid interface, inducing an indium-doped metallic surface layer of $VO_2$ (Fig. 1a). As a result, a visual colour change can be seen on the film surface after NaCl treatment (Fig. 1a, right). This approach effectively bypasses the Debye screening issue prevalent in current iontronics by utilizing the Helmholtz electric fields within the Debye length, thereby achieving a self-driven, bias-free operation. The kinetics of indium ion doping is governed by the interfacial electric fields, which, in turn, are determined by salt concentrations in the solution. Coupled with the ion-induced resistive memory effect, the indium/$VO_2$ system (hereafter referred to as the memsensor) senses salt solutions and simultaneously records its salt exposure history. These highly integrated functions mirror those of the amphid chemosensory neuron in the nematode *Caenorhabditis elegans*[21]. As a widely studied model organism in biological research, *C. elegans* is known for its simple but efficient nervous system with only 302 neurons[22]. Among these, the chemosensory neurons are pivotal in sensing and encoding exposure to salt, a key environmental cue associated with food abundance[21,22]. Specifically, the left amphid chemosensory neuron (ASEL) is responsible for detecting and memorizing increases in NaCl concentration[21], a process facilitated by $Ca^{2+}$ influx across the cellular membrane (Fig. 1b)[23]. This functionality differs from that of typical sensory neurons, which are capable of sensing but exhibit limited plasticity to memorize exposure history to environmental stimuli[24]. The integration of sensory input and memory demonstrated by the ASEL neuron is emulated in our memsensor device.

We first examine the basic electrical characteristics of the memsensor. Hall effect measurements (Fig. 1c) were conducted on two identical memsensors subjected to different NaCl concentrations. Each data point was obtained after the sample was rinsed and dried to eliminate the parasitic influence of solution on electrical measurements. The memsensors display non-volatile and accumulative conductivity enhancement with each NaCl treatment. Conversely, exposure to a diluted 0.03 wt% $H_2O_2$ solution gradually resets the conductivity to its initial value (Methods and Supplementary Fig. 2 show the $H_2O_2$ effect). Interestingly, during the NaCl exposure timeframe, conductivity increases almost linearly, with a steeper slope observed at higher NaCl concentration. We then performed four-probe measurements of the $VO_2$ resistance at different temperatures to confirm the insulator-to-metal phase transition in $VO_2$ induced by the NaCl treatments (Fig. 1d). Pristine $VO_2$ demonstrates a remarkable, three-orders-of-magnitude resistance change between the insulating and metallic phases, indicating the high quality of the film. A 0.1-M NaCl treatment for 90 s partially suppresses the phase transition, whereas a 3.4-M NaCl treatment for the same duration fully suppresses the phase transition, suggesting resistance dominated by the surface layer of the metallic phase in $VO_2$. In both cases, 0.03 wt% $H_2O_2$ treatment for approximately 120 s almost entirely resets the resistance state. The diluted $H_2O_2$ treatment was proven non-destructive to the $VO_2$ film within our experimental timeframe (Supplementary Fig. 3).

To investigate the mechanism of conductance change, we performed comprehensive characterization on the samples after solution treatment and surface rinsing. X-ray photoelectron spectroscopy (XPS) studies reveal the presence of indium ions on the clean regions of $VO_2$ film, away from indium metal, following NaCl treatments, as well as their subsequent removal following $H_2O_2$ treatments (Fig. 1e). X-ray absorption spectroscopy (XAS) results at the indium M edge indicate that indium is incorporated into the $VO_2$ lattice (Methods and Extended Data Fig. 1). Focusing on the vanadium valence state (Fig. 1f), we observe an increase in $V^{3+}$ weight after NaCl treatment and a return to $V^{4+}$ after $H_2O_2$ treatment, consistent with changes in the free electron concentration in the $VO_2$ film due to indium doping and extraction (Supplementary Fig. 4). The transmission electron microscopy (TEM) results (Fig. 1g,h) show that doping indium ions in $VO_2$ by NaCl immersion expands the spacing of (100) planes by 2.7%, and $H_2O_2$ treatment restores the spacing to the initial value (Supplementary Fig. 5). Our study confirms that the memsensor alters conductance through reversible ion transfer. It leverages the Helmholtz electric fields at the solid–liquid interface within the Debye length, distinct from the slower, voltage-biased ionic liquid gating approach used in previous works[2,9–12,15,17,18], achieving much enhanced switching speeds (~1 switch per second) under zero external bias (Fig. 1i).

## Memsensing mechanism

As shown in Fig. 2a, when $VO_2$ is immersed in the NaCl solution, an electric field arises at the solid–liquid interface. This field originates from the hydroxyl group termination on the $VO_2$ surface and its subsequent ionization (Methods provides details on the ionization of surface hydroxyl groups and zeta potential tests; Supplementary Fig. 6 and Supplementary Table 1). In response, an electric double layer spontaneously forms in the liquid adjacent to the $VO_2$ surface. The inner Helmholtz plane (IHP) and outer Helmholtz plane (OHP) make up the fixed layer, whereas mobile ions beyond the OHP form the diffuse layer. The thickness of this electric double layer corresponds to the Debye length, where the electric potential is linear in the fixed layer and saturates exponentially in the diffuse layer. As further explored, the spontaneous surface electric field is critical in facilitating ion doping into $VO_2$.

It is worth noting that immersing $VO_2$ alone in the NaCl solution does not change its conductance, highlighting the importance of indium in deriving the metallic phase of $VO_2$. Previous research[25] reported that electrochemical reactions between low-work-function metals and $VO_2$ in acids caused the hydrogenation of $VO_2$. However, our elastic recoil detection analysis (Supplementary Fig. 7) shows no increase in hydrogen concentration in $VO_2$ following NaCl exposure, thereby ruling out $VO_2$ hydrogenation in our case. The O K-edge soft XAS and X-ray emission spectroscopy (XES) studies confirm that NaCl treatment does not affect the electronic states of $VO_2$ via oxygen vacancies (Methods and Extended Data Fig. 2a,b show the oxygen-vacancy analysis). This result is corroborated by our density functional theory (DFT)-computed defect formation phase diagram (Fig. 2b), which shows that in the equilibrium limit (where $VO_2$ coexists with metallic indium and 0.1-M NaCl solution), the oxygen vacancy has a higher formation energy than both indium substitution and indium interstitial doping over a broad range of possible Fermi-level positions.

https://doi.org/10.1038/s41563-025-02312-9

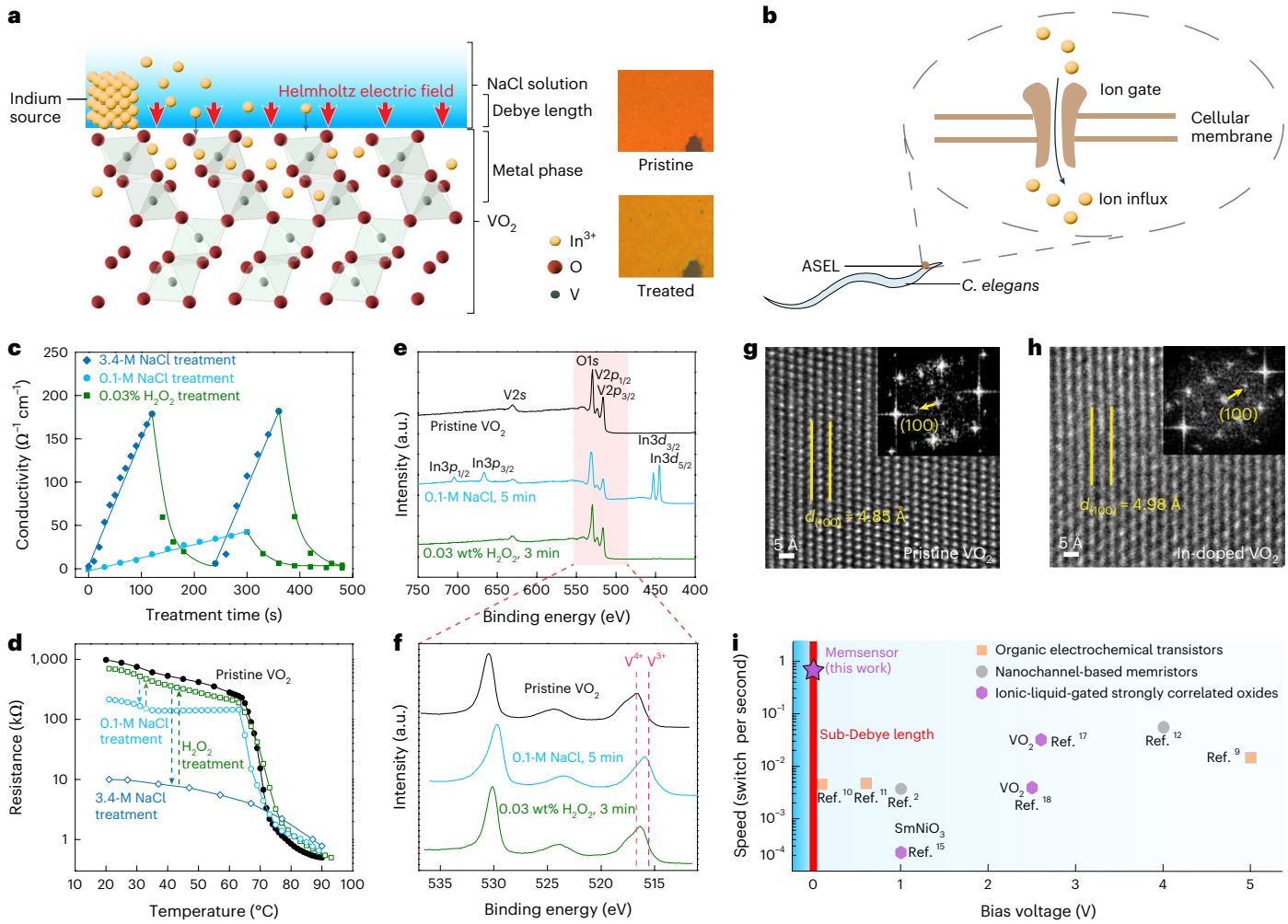


**Fig. 1 | High-speed, bias-free memsensor to mimic sensory neuroplasticity.** **a**, Schematic of the memsensor. $L \approx W \approx 0.5$ mm; $H \approx 0.1$ mm. Indium ions generated within the Debye screening length in the NaCl solution are driven into $VO_2$ by the Helmholtz electric field at room temperature, leading to an ultrathin, indium-doped metallic surface layer. An optical contrast is seen from the $VO_2$ surface post-NaCl immersion. **b**, With ion influx across the cellular membrane, the ASEL neuron in *C. elegans* senses and memorizes the salt exposure history, similar to the memsensor. **c**, Conductivity modulation of the memsensor by solution treatment. Data points are measured from the experiments and lines are included as a guide to the eye. **d**, Memsensor resistance versus temperature. **e**, XPS data confirming the indium doping post-NaCl treatment and extraction post-$H_2O_2$ treatment. **f**, Vanadium valence state reduced by NaCl treatment and recovered by $H_2O_2$ treatment. **g**,**h**, TEM images of pristine $VO_2$ (**g**) and $VO_2$ after NaCl treatment (**h**). **i**, Comparison of the memsensor with other iontronics, highlighting its operation at high switching speed and zero external bias.

Consequently, oxygen vacancy is unlikely to be the dominant defect type responsible for the observed electronic transition. Additionally, XAS measurements (Extended Data Fig. 2a,b) indicate that the bandgap of $VO_2$ thin films remains essentially unchanged after NaCl treatment. Electronic structure calculations further demonstrate that among the possible defect types at high concentrations, only indium interstitials introduce minimal perturbation to the fundamental bandgap of $VO_2$ (Extended Data Fig. 2c,d). Further analysis using XPS, scanning electron microscopy (SEM) and focused ion beam (FIB)–TEM confirms that indium is detectable in regions of $VO_2$ in which no surface precipitates are observed (Methods and Extended Data Fig. 3 show the precipitation analysis). Collectively, results from calculations and characterizations strongly suggest that the indium interstitial is probably the dominant defect.

As a low-work-function metal, indium transfers electrons to $VO_2$ and dissolves near the Helmholtz planes. Within the Helmholtz planes, the dissolved indium predominantly exists as $In^{3+}$ ions, as determined from the combined Pourbaix diagram and surface pH analysis, as well as from the hydrolysis analysis (Methods, Extended Data Fig. 4 and Supplementary Fig. 8). The electric field at the $VO_2$–NaCl interface subsequently drives the $In^{3+}$ ions into the $VO_2$ film, and their positive charges are neutralized by free electrons. The process can be summarized as follows:

$$c\mathrm{In} \rightarrow c\mathrm{In}^{3+} + 3ce^{-}, \quad (1)$$

$$\mathrm{VO_2} + c\mathrm{In}^{3+} + 3ce^{-} \rightarrow \mathrm{In}_c\mathrm{VO_2}. \quad (2)$$

The $In^{3+}$ generation followed by doping agrees well with the experimental results (Fig. 2c). We treated three samples with 0.1-M NaCl for 2 min, collected each solution onto a clean glass surface and analysed the indium ion in the residue post-water evaporation. XPS confirms indium ion generation after immersion of either the memsensor or In/Au/$VO_2$ in the NaCl solution (that is, indium was placed on top of a 70-nm-thick gold film on $VO_2$). On the contrary, when electron transfer between indium and $VO_2$ was blocked, no indium ions were produced in the solution. Furthermore, although indium ions were formed in deionized (DI) water after a 2-min immersion of the memsensor (Fig. 2d), they could hardly dope into the $VO_2$ film (Fig. 2d and

https://doi.org/10.1038/s41563-025-02312-9

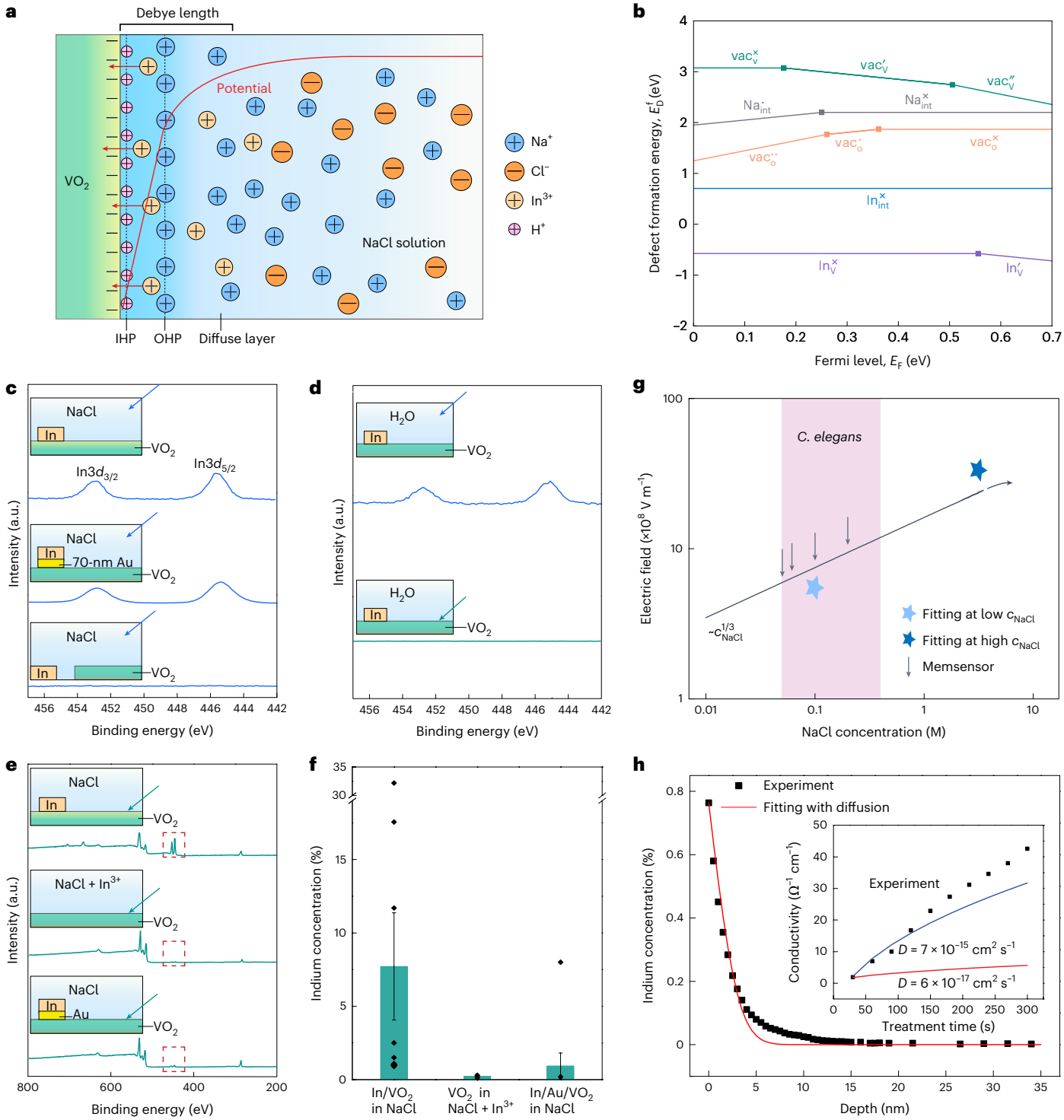


**Fig. 2 | Mechanism and kinetics of the memsensor. a**, Schematic of the oxide–liquid interface. **b**, DFT-calculated defect formation energies ($E_D^f$) with respect to the Fermi level ($E_F$). In the Kröger–Vink notation, vac and int denote vacancies and interstitials, respectively. **c**, Indium ion generation analysis, where the two peaks are from In3$d_{3/2}$ and In3$d_{5/2}$, indicating that the $In^{3+}$ ions are generated only when In metal is electrically connected to $VO_2$. Blue arrow towards the solution: XPS test on the drop-cast and dried solution. **d**, Analysis in the absence of surface electric fields in DI water, indicating that $In^{3+}$ ions are generated in the liquid but not driven into $VO_2$ in DI water. Green arrow towards $VO_2$: XPS test on $VO_2$ surface. **e**, Influence of ion–$VO_2$ surface distance on indium ion doping, indicating the necessity of $In^{3+}$ ion generation within the Debye length. **f**, Indium ion concentrations measured at nine evenly distributed surface points on each $VO_2$ sample shown in **e**. Data are presented as mean ± standard error of the mean ($n$ = 9 technical replicates per sample). **g**, Calculated surface electric fields. Stars, electric fields extracted from fitting the data in Fig. 1c; arrows, memsensor mimicking plasticity in a salinity range where *C. elegans* is active (Fig. 3). **h**, Fitting the XPS-measured $In^{3+}$ depth profile (main) and compared with conductivity transient (inset) with ion diffusion only.

Extended Data Fig. 5a). This is attributed to the absence of electric fields at the $VO_2$–DI water interface, which is necessary to drive $In^{3+}$ ions into the $VO_2$ film.

In particular, following NaCl exposure, sodium signals were strikingly absent in $VO_2$ compared with indium (Extended Data Fig. 5b). Angle-resolved XPS (ARXPS) indicates very limited sodium doping

at the shallow surface of $VO_2$, whereas indium exhibits much deeper penetration (Extended Data Fig. 5c,d). This result is consistent with the defect formation phase diagram (Fig. 2b), which demonstrates that when $VO_2$ is at equilibrium with metallic indium and 0.1-M NaCl solution, sodium doping has considerably higher formation energy and, consequently, lower propensity to form than indium doping. The different doping levels of sodium and indium prompted further examination of ion doping conditions. In Fig. 2e, immersing the memsensor in a NaCl solution resulted in indium doping in $VO_2$, and the solution with the generated $In^{3+}$ ions (NaCl + $In^{3+}$) was used to immerse a $VO_2$ film alone without indium metal, resulting in significantly less indium doping. Similarly, in the In/Au/$VO_2$ setup, despite the formation of $In^{3+}$ ions in the solution (Fig. 2c), only a very low concentration of these ions was doped into $VO_2$. Analysis of the average indium concentration on each of these $VO_2$ films further confirmed the observation (Fig. 2f). These results suggest that it is critical to generate $In^{3+}$ ion in close proximity to the $VO_2$ surface for doping. As depicted in Figs. 1a and 2a and Methods, only the ions formed within the Debye screening length experience a strong electric field, driving them into $VO_2$, whereas those outside the OHP feel a diminished electric field, limiting their doping into the $VO_2$ surface.

## Memsensing dynamics

The strength of the surface electric field is calculated with surface chemistry and electrostatics. An approximate analytical solution is presented in Fig. 2g (Methods and Extended Data Fig. 6a show the calculation model). At high NaCl concentrations, the electric field approaches a maximum, which is related to the equilibrium constant (pK; estimated to be 4.5 ± 0.9 through titration; Methods and Extended Data Fig. 6b–d) of the surface reaction and is independent of the NaCl concentration ($c_{NaCl}$). At low NaCl concentrations, the electric field is proportional to $c_{NaCl}^{1/3}$, showing sensitivity of our memsensor in the low-salt-concentration range that *C. elegans* responds to[24].

XPS combined with surface argon sputtering was used to investigate the dynamics of indium ion doping in $VO_2$. Following a 0.1-M NaCl treatment for 5 min, the atomic fraction of indium ($c$) along the depth of $VO_2$ was measured (Fig. 2h; more depth profile fitting scenarios after NaCl treatment with other times are shown in Supplementary Fig. 9). The diffusive depth profile was then fitted to the solution of Fick's second law of diffusion as $\frac{dc}{dt} = D\frac{d^2c}{dx^2}$, where $D$ is the diffusivity of indium in $VO_2$ and is approximately $6 \times 10^{-17}$ cm$^2$ s$^{-1}$ (Methods provides the depth profile fitting details). Each indium ion introduces three electrons into the $VO_2$ film, gradually increasing its conductivity over time during NaCl immersion. However, simulations based solely on indium ion diffusion fail to fully reproduce the experimental conductivity, as evidenced by the mismatch between the nonlinearity of Fick's second law solution and the nearly linear conductivity increase (Fig. 2h, inset). To address this discrepancy, we recognize the importance of considering ion drift under the surface electric field ($E$) and modify the Fick's second law as

$$\frac{\partial c}{\partial t} = D\frac{\partial^2 c}{\partial x^2} - \mu E\frac{\partial c}{\partial x} - \mu c\frac{\partial E}{\partial x}, \quad (3)$$

where $\mu$ is the indium ion mobility in $VO_2$. The initial condition is $c(x, t = 0) = c_0(x) = \begin{cases} c_{surface} & (\text{surface}, x = 0) \\ 0 & (VO_2 \text{ bulk}, x > 0) \end{cases}$. Assuming a homogeneous $E$ and in the absence of diffusion ($D = 0$), it can be seen that $c(x, t) = c_0(x - \mu Et)$, implying that the concentration profile at time $t$ is just a spatial translation of the initial condition along the $x$ axis. Hence, the total indium dose doped in $VO_2$, that is, the area enclosed by $c(x, t)$ and the $x$ axis, increases linearly with time, leading to a nearly linear correlation between the conductivity and treatment time (Fig. 1c). To accurately simulate the indium concentration distribution and evolution, diffusion must still be considered, as the depth profile exhibits a long tail (Fig. 2h). Using a constant-concentration boundary condition, numerical simulations incorporating both ion drift and ion diffusion effectively fit the experiments in Fig. 1c (Extended Data Fig. 7; Methods and Supplementary Fig. 10 show the fitting with diffusion and drift in more detail). The electric fields derived from the fittings and predicted by the analytical model (Fig. 2g) are summarized in Supplementary Table 2. The numerical simulation model of equation (3) was also solved using a constant-flux boundary condition. The analysis is provided in the Methods, and the corresponding simulation results are shown in Supplementary Fig. 11.

## Memsensors mimicking gustatory neuroplasticity

Extending the duration of NaCl treatment results in a gradual saturation of $VO_2$ conductance after the initial linear increase (Extended Data Fig. 8). The sensing, memory and adaptability of the memsensor pave the way for a variety of bioinspired applications. Our study draws a parallel between the memsensor's electrical behaviour and the gustatory neural response of *C. elegans* in similar salinities (Fig. 2g). In Fig. 3a, the brown curves in the insets represent $Ca^{2+}$ transients in the ASEL as the response signal, reproduced from a previous report[24]. Initially, the response to second-round NaCl exposure increases with the increased duration of first-round NaCl exposure; it then diminishes with prolonged first-round exposure, ultimately becoming non-responsive, indicating full adaptation to the specific NaCl concentration. Similarly, in our memsensor, conductance change first increases with prior immersion time and then decreases with prolonged prior immersion, eventually stabilizing. Figure 3b illustrates the memsensor's ASEL-like responses to different NaCl concentrations. After adaptation to 100-mM NaCl, a slight increase in concentration fails to activate the ASEL, whereas a substantial increase does. Likewise, post-stabilization in 50-mM NaCl, the memsensor remains unresponsive to 60-mM NaCl, but responds to higher concentrations. As the ASEL becomes non-responsive after extended exposure time, we use $\partial C/\partial t$ to replicate the ASEL response (Fig. 3c), where $C$ represents the memsensor's electrical conductance.

In *C. elegans*, the ASEL responds to rising NaCl concentration, whereas the right-side sensory neuron (ASER) detects and encodes decreasing NaCl levels. Their collaboration dictates the worm's movement along or against the salt gradient, known as chemotaxis[26]. Neuroplasticity in these sensory neurons enables the worm to link salt concentration with food availability, adapting its chemotaxis strategy accordingly[27]. Our memsensor also emulates the ASER's response between the on and off states of NaCl exposure through $H_2O_2$ resetting. In Fig. 3d, the insets depict the ASER responses to varying NaCl exposure times as the environment switches from NaCl to water[24]. Prolonged NaCl exposure sensitizes the ASER, leading to increased response intensity during the NaCl-off period. Similarly, longer NaCl treatment lowers the memsensor's resistance, amplifying resistance increase during the NaCl-off period (that is, when the memsensor is treated with $H_2O_2$). In Fig. 3e, $\partial R/\partial t$ mimics the ASER response during the NaCl-off state, where $R$ is the resistance of the memsensor.

Adaptive chemotaxis enables *C. elegans* to navigate the landscape of varying NaCl concentrations and food availability. The replication of chemotaxis has inspired robotic target searches in unknown environments and chemical distribution mapping[28,29]. Our memsensor closely resembles the ASEL response to NaCl increase, enabling the replication of *C. elegans*' foraging behaviour in our demonstration device. A miniature boat equipped with memsensors is compared with an identical boat mounted with conventional, non-memory NaCl sensors, where each non-memory sensor is a pair of electrodes directly measuring the liquid resistance (Methods and Extended Data Fig. 9 show the boat fabrication and Extended Data Fig. 10 shows the circuit design). In Fig. 4a, once *C. elegans* learns to associate high NaCl levels with starvation, it avoids such concentrations in

https://doi.org/10.1038/s41563-025-02312-9

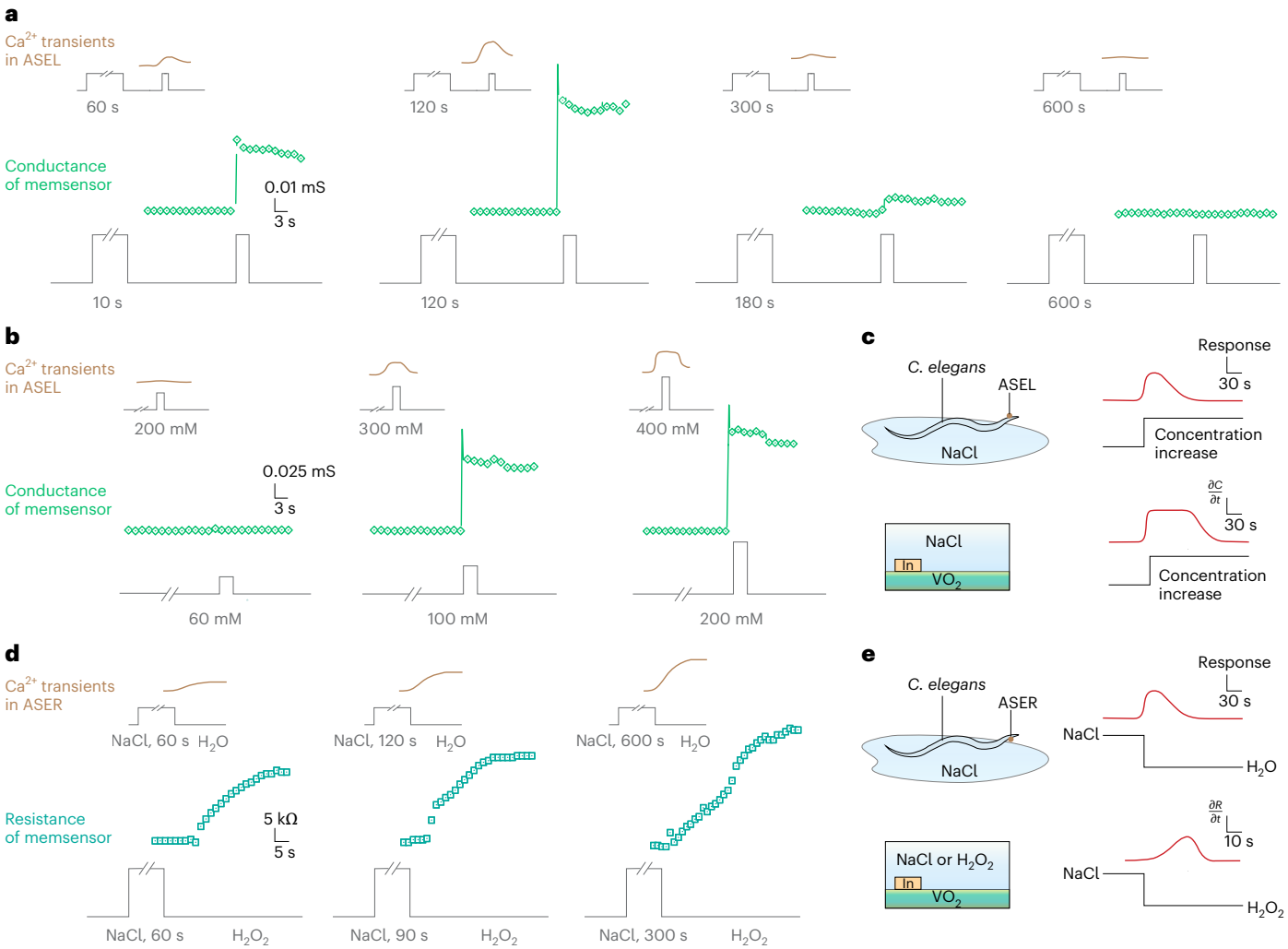


**Fig. 3 | Memsensor mimicking sensory neuroplasticity. a**, Conductance (*C*) mimicking the ASEL's time-dependent response. *C. elegans* pre-exposed to 100-mM NaCl for different durations, washed for 60 s and then exposed to 100-mM NaCl for 3 s. Memsensors pre-exposed to 50-mM NaCl for different times, washed for 20 s and exposed to 50-mM NaCl for 3 s, with conductance monitored in real time. **b**, Mimicking the ASEL's concentration-dependent response. *C. elegans* pre-exposed to 100-mM NaCl for 600 s and then exposed to different concentrations for 3 s. Memsensors pre-exposed to 50-mM NaCl for 600 s and then exposed to different NaCl concentrations for 3 s. **c**, $\partial C/\partial t$ of memsensors mimics the ASEL's response with long high-concentration duration. **d**, Mimicking the ASER's sensitization. A longer exposure in 100-mM NaCl sensitizes the ASER and amplifies resistance increase in memsensors during $H_2O_2$ treatment. **e**, $\partial R/\partial t$ mimics the ASER's response with long NaCl-off duration. Insets in **a**, **b** and **d** adapted from ref. 24 under a Creative Commons license CC BY 4.0.

new environments, with the ASEL neurons suppressing the typical response to increased NaCl (ref. 30). Conversely, after prolonged exposure to low NaCl concentrations without food, *C. elegans* exhibits attraction to higher concentrations in new environments[30]. To demonstrate aversion to high concentrations, the memsensor is conditioned in 400-mM NaCl (high concentration) for 40 min, after which it learns to avoid high concentrations by desensitizing its conductance to NaCl. The memsensor-equipped boat is then placed in a 50-mM (low-concentration) NaCl zone separated with a barrier from the 400-mM NaCl zone. On barrier removal, the boat shows no response to the increased NaCl concentration and, hence, is not misguided to the 'food-absent' high-concentration zone (Fig. 4b and Supplementary Video 1). By contrast, the boat equipped with non-memory sensors detects the increased concentration and immediately moves towards the food-absent high-concentration zone. In all trials, neuroplasticity of the memsensors consistently functions to eliminate the risk of guiding the boat into food-absent zones (Fig. 4c). To demonstrate attraction to high concentrations, the memsensor-equipped boat is conditioned in 50-mM NaCl for 120 min to stabilize the $VO_2$ conductance, after which it navigates away from the low-concentration zone towards the high-concentration region (Fig. 4d and Supplementary Video 2). The mimicked neuroplasticity successfully directed the boat to the preferred 'food-abundant' high NaCl concentrations in eight out of ten attempts (Fig. 4e). By contrast, the boat mounted with non-memory sensors is always misled into the food-absent low-concentration zone (Supplementary Fig. 12). It should be noted that both high response speed and bias-free nature of the memsensor are vital to imitate the adaptive chemotaxis.

In this study, a high-speed, bias-free memsensor operating within the Debye screening length is presented. The atomic mechanism is elucidated as the electrochemical generation of dopant ions followed by their diffusion and drift driven by built-in electric fields within the Debye length. The memsensor closely resembles the sensory neuroplasticity in *C. elegans* with respect to NaCl exposure and enables a microrobotic boat to replicate the adaptive chemotaxis in a complex NaCl landscape. Our study inspires neurorobotics with simpler and more compact design, lower energy footprint and capability of navigating fields with complex chemical gradients. It also holds promise for creating neuromorphic computing architectures through iontronic devices with purely inorganic components.

https://doi.org/10.1038/s41563-025-02312-9

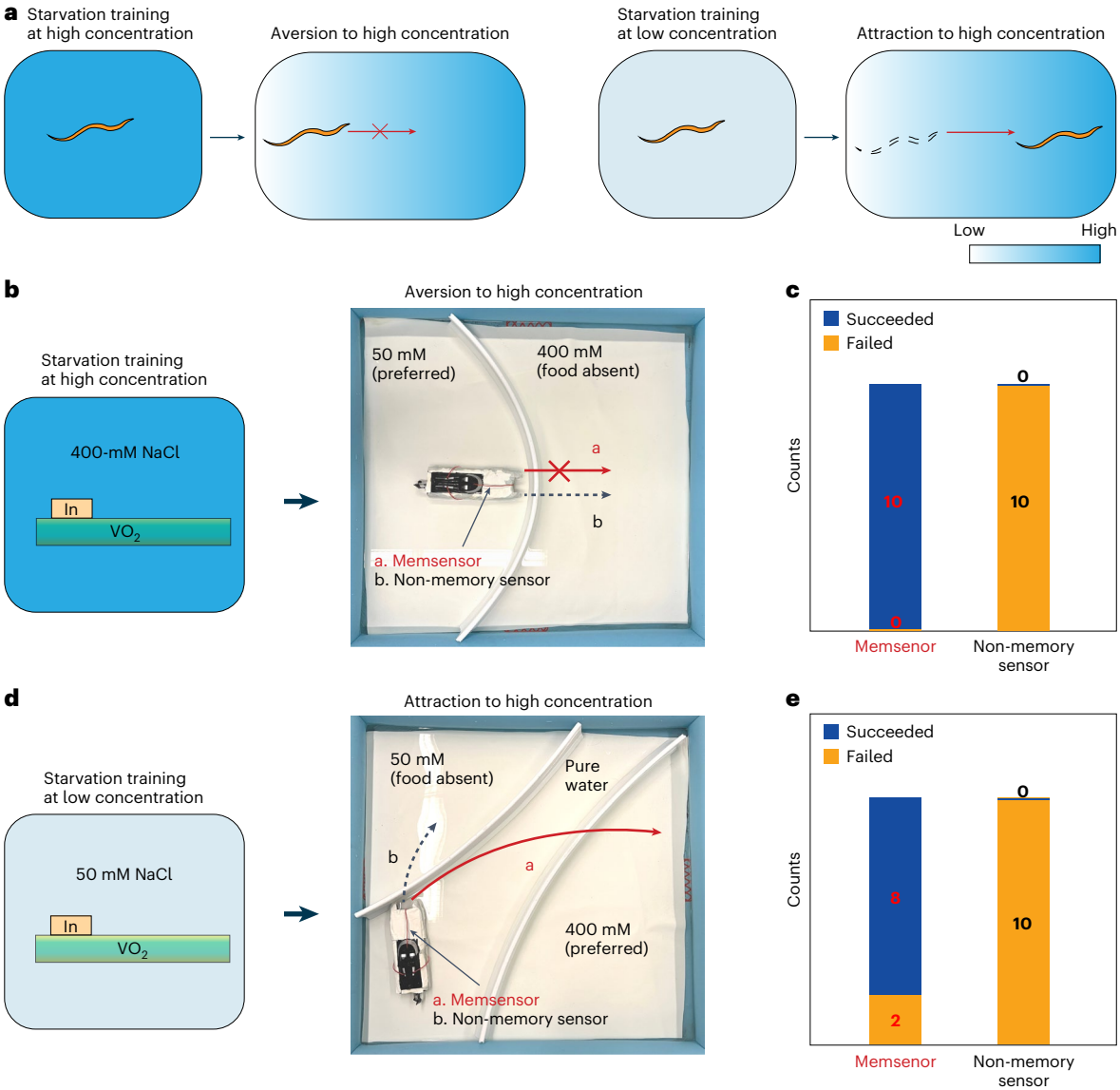


**Fig. 4 | Demonstration of adaptive chemotaxis using the ASEL-like neuroplasticity of memsensors. a**, Adaptive chemotaxis of *C. elegans* after cultivation in high or low salt concentrations without food. **b**, After 'starvation' training in high NaCl concentration, the memsensor-equipped boat avoids entering high-concentration zones, whereas the non-memory boat sails there. **c**, Memsensors reliably prevent misdirection to high-concentration food-absent areas compared with non-memory sensors. **d**, After starvation training in low concentration, the memsensor-equipped boat exhibits chemotaxis to the preferred high-concentration zones, whereas the non-memory boat sails to low concentrations. **e**, The memsensor-equipped boat successfully navigates to the preferred zone in eight out of ten attempts, whereas the non-memory boat consistently sails to the undesired, food-absent area.

## Online content

Any methods, additional references, Nature Portfolio reporting summaries, source data, extended data, supplementary information, acknowledgements, peer review information; details of author contributions and competing interests; and statements of data and code availability are available at https://doi.org/10.1038/s41563-025-02312-9.

## References


1. Robin, P., Kavokine, N. & Bocquet, L. Modeling of emergent memory and voltage spiking in ionic transport through angstrom-scale slits. *Science* **373**, 687–691 (2021).
2. Robin, P. et al. Long-term memory and synapse-like dynamics in two-dimensional nanofluidic channels. *Science* **379**, 161–167 (2023).
3. Zhang, Z. et al. Perovskite nickelates as electric-field sensors in salt water. *Nature* **553**, 68–72 (2018).
4. Jayachandran, D. et al. A low-power biomimetic collision detector based on an in-memory molybdenum disulfide photodetector. *Nat. Electron.* **3**, 646–655 (2020).
5. Ahmed, D. et al. Bioinspired acousto-magnetic microswarm robots with upstream motility. *Nat. Mach. Intell.* **3**, 116–124 (2021).
6. Debanne, D., Inglebert, Y. & Russier, M. Plasticity of intrinsic neuronal excitability. *Curr. Opin. Neurobiol.* **54**, 73–82 (2019).
7. Chun, H. & Chung, T. D. Iontronics. *Annu. Rev. Anal. Chem.* **8**, 441–462 (2015).
8. Bisri, S. Z., Shimizu, S., Nakano, M. & Iwasa, Y. Endeavor of iontronics: from fundamentals to applications of ion-controlled electronics. *Adv. Mater.* **29**, 1607054 (2017).
9. Van Doremaele, E. R. W., Ji, X., Rivnay, J. & Van De Burgt, Y. A retrainable neuromorphic biosensor for on-chip learning and classification. *Nat. Electron.* **6**, 792–800 (2023).

10. Van De Burgt, Y. et al. A non-volatile organic electrochemical device as a low-voltage artificial synapse for neuromorphic computing. *Nat. Mater.* **16**, 414–418 (2017).
11. Xie, K. et al. Organic electrochemical transistor arrays for real-time mapping of evoked neurotransmitter release in vivo. *eLife* **9**, e50345 (2020).
12. Zhang, P. et al. Nanochannel-based transport in an interfacial memristor can emulate the analog weight modulation of synapses. *Nano Lett.* **19**, 4279–4286 (2019).
13. Xiong, T. et al. Neuromorphic functions with a polyelectrolyte-confined fluidic memristor. *Science* **379**, 156–161 (2023).
14. Ding, K. et al. Phase-change heterostructure enables ultralow noise and drift for memory operation. *Science* **366**, 210–215 (2019).
15. Shi, J., Ha, S. D., Zhou, Y., Schoofs, F. & Ramanathan, S. A correlated nickelate synaptic transistor. *Nat. Commun.* **4**, 2676 (2013).
16. Park, T. J. et al. Complex oxides for brain-inspired computing: a review. *Adv. Mater.* **35**, 2203352 (2023).
17. Jeong, J. et al. Suppression of metal-insulator transition in $VO_2$ by electric field-induced oxygen vacancy formation. *Science* **339**, 1402–1405 (2013).
18. Zhou, Y. et al. Control of emergent properties at a correlated oxide interface with graphene. *Nano Lett.* **15**, 1627–1634 (2015).
19. Wang, S. et al. An organic electrochemical transistor for multi-modal sensing, memory and processing. *Nat. Electron.* **6**, 281–291 (2023).
20. Vahl, A. et al. Concept and modelling of memsensors as two terminal devices with enhanced capabilities in neuromorphic engineering. *Sci. Rep.* **9**, 4361 (2019).
21. Suzuki, H. et al. Functional asymmetry in *Caenorhabditis elegans* taste neurons and its computational role in chemotaxis. *Nature* **454**, 114–117 (2008).
22. Appleby, P. A. A model of chemotaxis and associative learning in *C. elegans*. *Biol. Cybern.* **106**, 373–387 (2012).
23. Ferkey, D. M., Sengupta, P. & L'Etoile, N. D. Chemosensory signal transduction in *Caenorhabditis elegans*. *Genetics* **217**, iyab004 (2021).
24. Dekkers, M. P. J. et al. Plasticity in gustatory and nociceptive neurons controls decision making in *C. elegans* salt navigation. *Commun. Biol.* **4**, 1053 (2021).
25. Chen, Y. et al. Non-catalytic hydrogenation of $VO_2$ in acid solution. *Nat. Commun.* **9**, 818 (2018).
26. Queirós, L. et al. Overview of chemotaxis behavior assays in *Caenorhabditis elegans*. *Curr. Protoc.* **1**, e120 (2021).
27. Park, C. et al. Roles of the ClC chloride channel CLH-1 in food-associated salt chemotaxis behavior of *C. elegans*. *eLife* **10**, e55701 (2021).
28. Jiang, L., Mo, H. & Tian, P. A bacterial chemotaxis-inspired coordination strategy for coverage and aggregation of swarm robots. *Appl. Sci.* **11**, 1347 (2021).
29. Nurzaman, S. G., Matsumoto, Y., Nakamura, Y., Koizumi, S. & Ishiguro, H. 'Yuragi'-based adaptive mobile robot search with and without gradient sensing: from bacterial chemotaxis to a Levy walk. *Adv. Robot.* **25**, 2019–2037 (2011).
30. Kunitomo, H. et al. Concentration memory-dependent synaptic plasticity of a taste circuit regulates salt concentration chemotaxis in *Caenorhabditis elegans*. *Nat. Commun.* **4**, 2210 (2013).

## Methods

### Sample preparation

All samples were prepared in the Marvell Nanofabrication Laboratory at UC Berkeley. The 75-nm $VO_2$ thin films were grown on a thermal oxide silicon wafer using a reactive sputtering method. A vanadium target was used. The power was set to 200 W. The films were deposited in 60-s.c.c.m. argon with 6.05-s.c.c.m. $O_2$ environment at room temperature for 10 min. Subsequently, a post-deposition annealing process was performed in the sputtering chamber in 120-s.c.c.m. $O_2$ environment at 580 °C for 30 min.

In the Hall effect measurements (Fig. 1c) and four-probe measurements (Fig. 1d), 500 µm × 500 µm-sized Ti/Au electrodes were sputtered on 1.5 cm × 1.5 cm $VO_2$ samples for precise testing. Electrode patterns were created by standard photolithography. Following the lift-off process, $VO_2$ with Ti/Au at four corners were prepared. A small piece of indium (diameter, ~500 µm) was cut from an indium bead and pressed onto the centre of $VO_2$ to form the memsensor. In other experiments, indium pieces were directly used as electrodes on $VO_2$ for ease of study.

### XPS

XPS experiments were performed on the PHI 5800 X-ray photoelectron spectrometer in the California Institute for Quantitative Biosciences at UC Berkeley. The survey spectra were collected using a pass energy of 187 eV with 0.8 eV per step. High-resolution spectra were collected using a pass energy of 46.95 eV with 0.1 eV per step. In high-resolution testing, C1*s* (284.8 eV) was always selected to calibrate the spectra. Depth profile was achieved using argon sputtering to etch the $VO_2$ surface. The beam voltage was set to 5 kV and the ion current was 1 µA. $VO_2$ etching rate was 0.5 nm $min^{-1}$. After each minute of sputtering, XPS analysis was conducted to monitor and characterize the surface composition.

### XAS and XES

Soft XAS and XES measurements were performed at the iRIXS endstation of the Advanced Light Source at Lawrence Berkeley National Laboratory, with details of the system and spectrometer parameters reported previously[31]. The energy resolution of both O K and In M XAS spectra was about 0.2 eV without considering the core-hole broadening effect. O K XES spectra were collected at an excitation energy of 560 eV and dwell time of 10 min, with an emission energy resolution of about 0.33 eV.

### TEM and FIB–TEM

$VO_2$ samples were immersed in a buffered oxide etchant solution with 6:1 volume ratio of 40% $NH_4F$ to 49% HF. The $SiO_2$ layer was etched after soaking in the buffered oxide etchant for 10 min, and floating $VO_2$ fragments were carefully salvaged using a pipette and transferred into water. Following a thorough cleaning in water, the fragments were deposited onto copper grids for TEM study. The TEM experiments were performed on a Thermo Fisher Scientific ThemIS aberration-corrected transmission electron microscope at the Molecular Foundry, Lawrence Berkeley National Laboratory. The microscope was operated at 300 keV with a high-speed Ceta2 scintillator-coupled complementary metal–oxide–semiconductor camera. The TEM images were analysed using the ImageJ software (version 1.54g). Real-space images underwent fast Fourier transformation. The $VO_2$ diffraction patterns were simulated using the SingleCrystal software (version 5.2.1). The fast Fourier transform patterns were then compared with the simulated diffraction patterns to index the crystal planes and calculate the interplanar distances.

For FIB–TEM, a thin lamella (~80 nm) of the sample was prepared for TEM analysis using the Thermo Scientific Scios 2 DualBeam FIB-SEM system. To protect the surface, a platinum layer was first deposited, followed by lamella preparation using a gallium-ion-based FIB lift-out process. Initial trenching and rough milling were performed at an acceleration voltage of 30 kV and a beam current of 5 nA, whereas thinning and fine polishing were carried out at 5 kV and 0.15 nA to minimize ion-induced damage. TEM characterization was conducted on an FEI Titan 60-300 microscope operated at 300 kV at the National Center for Electron Microscopy, Lawrence Berkeley National Laboratory.

### ARXPS

ARXPS was performed on a Thermo Fisher Nexsa device in Cerium Laboratories. The pass energy was 50 eV for high-resolution scans. The take-off angle ranged from 1.4° (nominally, 0°) to 51° (nominally, 52.4°).

### Elastic recoil detection analysis

Elastic recoil detection analysis, also known as forward scattering, was done in Cerium Laboratories. Here a 1.9-MeV $^4He^+$ beam was used to bombard the sample surface. A foil with a thickness of 8.5 µm was used in front of the recoil detector to block the forward-scattered α-particles.

### Atomic force microscopy

Atomic force microscopy images were obtained in the tapping mode using a Veeco multimode atomic force microscope.

### Raman spectroscopy

Raman spectroscopy was conducted using a Renishaw confocal micro-Raman microscope with a laser excitation wavelength of 488 nm, a ×100 objective (numerical aperture of 0.95; laser spot size of ~1 µm) and a 2,400 l $mm^{-1}$ grating.

### Hall effect measurements

The conductivity and charge carrier concentrations were determined using the ECOPIA Hall effect measurement system HMS-3000 in Building 2, Lawrence Berkeley National Laboratory. The magnetic-field intensity was set at 0.55 T. Each conductivity in this study was averaged over three measurements.

### Absence of effects of oxygen vacancies on electron states as evidenced from O K-edge soft XAS and XES data

XAS provides insights into the local density of unoccupied electronic states, whereas XES reveals the local density of occupied electronic states. As established in another work[32], O K-edge XES and O1*s* XAS measurements are effective and sensitive ways for probing the electronic structure and oxygen-vacancy concentration of strongly correlated oxides.

We performed O K-edge soft XAS and XES measurements of the $VO_2$ films. As shown in Extended Data Fig. 2a,b, the XAS and XES spectra for indium-attached $VO_2$ after NaCl treatment are represented by the red lines. Compared with the spectra collected from $VO_2$, there is negligible difference between the spectra beyond the experimental system error. The results are consistent in both total-electron-yield and total-fluorescence-yield modes.

These results suggest that changes in oxygen vacancies are negligible. Previous studies[33,34] have shown that an increase in oxygen vacancies results in a shift of the XAS peak to a lower energy as well as a narrower bandgap. However, in our case, no such XAS peak shift is observed, and the bandgap (which can be estimated by the gap between the tangent lines of XES and XAS) is not reduced after NaCl treatment. These suggest that the change in oxygen vacancies is either absent or present in negligible amounts.

### Absence of indium precipitation in $VO_2$

**XPS analysis.** To ensure accurate results, regions with a residual indium patch on top were physically separated from those without, similar as the procedure used in the XAS of indium and other XPS measurements. XPS analysis was performed on clean regions of the $VO_2$ film that did

not contain any indium residue. The XPS results confirmed that indium is present in $VO_2$ (Extended Data Fig. 3a).

**SEM analysis.** To determine whether indium forms precipitates on the $VO_2$ surface, we conducted detailed SEM analysis on the sample (Extended Data Fig. 3a). SEM images of pristine sputtered $VO_2$ and $VO_2$ after NaCl treatment are shown in Extended Data Fig. 3b,c. The images demonstrate that the $VO_2$ surface remains clean and free of any visible precipitates after the treatment, despite the presence of indium signal detected by XPS.

**FIB–TEM analysis.** Further investigation using FIB–TEM confirmed the absence of precipitation on the $VO_2$ surface. The TEM sample was prepared using FIB, and SEM imaging during the lift-out process showed no visible precipitates (Extended Data Fig. 3d). To protect the $VO_2$ surface, a layer of platinum was deposited using an electron beam, followed by an additional layer deposited with an ion beam. Cross-sectional TEM images further corroborated the absence of precipitates on the $VO_2$ surface (Extended Data Fig. 3e,f).

### XAS analysis at the indium M edge

We have performed XAS measurements for the indium M edge from a treated $VO_2$ film and an indium metal (indium patch), with the results presented in Extended Data Fig. 1. The black curve corresponds to the indium patch, whereas the red curve represents the $VO_2$ surface after NaCl treatment. As mentioned in the XPS study in the 'Absence of indium precipitation' section, the $VO_2$ sample used for plotting the red curve in Extended Data Fig. 1 was physically separated from the regions containing residual indium metal on the surface.

The spectrum collected on the surface of the indium metal displayed a typical rising edge at a low energy of 443.5 eV, corresponding to the metal. The second rising edge near 450 eV, along with subsequent oscillation peaks, indicates the presence of $In_2O_3$, which is expected on the indium surface when exposed to air. In sharp contrast, the red curve from the $VO_2$ surface shows no indium metal signal, confirming that indium does not segregate into metallic precipitates on/in the $VO_2$ surface. Furthermore, the line shape of the red curve differs from the oxide features in the black curve and appears sharper, despite the fact that the experimental resolution is identical. This suggests that indium is atomically incorporated into a more well-defined crystal field, that is, the $VO_2$ lattice, rather than existing as surface oxides.

### Titration

Here 1 g of $VO_2$ powder was introduced into a 50-ml solution of either 0.01-M or 0.001-M NaCl to form a suspension. The mixture was continuously stirred overnight at room temperature to reach equilibrium of the deprotonation reaction. Subsequently, a 0.1-M NaOH solution was incrementally added in drops of 0.05 ml each to the suspension, and the corresponding pH values of the suspension were recorded. The measured pH curves are fitted to estimate the equilibrium constant pK ($pK = -\log_{10}[K]$) of the surface deprotonation reaction. Additional details on the titration data fitting are provided in the calculation model below.

### Zeta potential tests

Zeta potential tests were completed in Covalent Metrology. The dispersed $VO_2$ particles were filtered from the solution using a CFP5-grade filter with a pore size of 2.5 µm. The powder was then packed into a cylindrical measurement cell, sandwiched between 10-µm filters and rinsed with DI water to remove any excess sample particles larger than 10 µm. The zeta potential was measured via streaming potential using an Anton Paar SurPASS3 instrument. Ten measurements were performed, and the reported zeta potential is the average of the last five measurements. This process was repeated for samples with NaCl concentrations of 0.01 M, 0.1 M and 1 M.

### Boat integrated with memsensors: boat fabrication and circuit design

To achieve optimal mechanical balance among all the electrical components, a toy boat was used. The toy boat came equipped with a battery, a d.c. motor, a servo motor, a propeller and a rudder, offering a convenient platform for maintaining mechanical balance. The original controller was replaced with two Arduino Nano 33 IoT boards (Extended Data Fig. 9a). Board 1 was used to control the d.c. motor for propelling the boat forward, whereas Board 2 managed the servo motor for steering the boat right or left. Given the high-power requirement of the d.c. motor, a motor driver was used to establish a connection between the d.c. motor and Board 1. The original battery was repurposed to charge Board 2 and the motor driver, whereas an additional battery was used to power Board 1.

The boards controlled the d.c. motor and the servo motor through voltage divider circuits. Three memsensors were attached to the bottom of the boat (Extended Data Fig. 9b). Wire–$VO_2$ contact areas and wire connection areas are carefully sealed with adhesives to minimize the influence of solution conductance.

In Extended Data Fig. 10a, the front memsensor was connected to a 400-kΩ resistor in series (Extended Data Fig. 10a, $R_0$), and the voltage difference on the memsensor over a certain duration was transmitted to the Arduino board to regulate the d.c. motor. Extended Data Fig. 10b shows the algorithm that processes data. Changes in the memsensor's resistance are detected by reading the analogue pin $A_0$ on the Arduino board ($V_{OUT}$), which then triggers the pulse-width modulation (PWM) signal on pin D6 to control the d.c. motor. To be more specific, the voltage at $A_0$ is sampled at regular time intervals, and each reading is compared with the previous one. As detailed in this figure, if the voltage decreases by $\Delta V$, exceeding a predefined threshold, the PWM signal generates an output voltage proportional to $\Delta V$, calculated as constant × $\Delta V$, to adjust the motor's rotational speed. Since the d.c. motor in this study requires a voltage higher than the Arduino board can provide, a motor driver is incorporated into the circuit (Extended Data Fig. 10a).

Extended Data Fig. 10c illustrates the control mechanism for left and right turns. Similar to the setup in Extended Data Fig. 10a, the left and right memsensors are each part of their respective voltage divider circuits. Extended Data Fig. 10d shows the algorithm that processes data. The voltages at analogue pins $A_0$ and $A_1$ are sampled at regular intervals, and the changes in voltage, $\Delta V_{left}$ and $\Delta V_{right}$, are calculated and compared. If $\Delta V_{left} - \Delta V_{right}$ exceeds a predefined threshold, the PWM signal adjusts the servo motor to a specific angle, turning the rudder to the left. Conversely, if $\Delta V_{right} - \Delta V_{left}$ exceeds the threshold, the PWM signal adjusts the servo motor to a different angle, turning the rudder to the right. If the difference between $\Delta V_{left}$ and $\Delta V_{right}$ is within the threshold, the boat maintains its current direction without turning.

### Boat integrated with non-memory sensors

The mechanical structure and circuit design of the boat featuring non-memory sensors are similar to those of a boat equipped with memsensors (Extended Data Fig. 9c,d). There are two primary differences: each memsensor is replaced by two stainless steel rods as electrodes to measure the conductance of the solution between them; to prevent any electrolysis effect in the solution, fixed resistors with higher resistance values (~1–2 MΩ) are used (Extended Data Fig. 10a,c; $R_0$).

### $H_2O_2$ effect

We analysed the decrease in conductivity following the immersion of the sample in a 0.03 wt% $H_2O_2$ solution. As the nonlinear trend over time suggests a minor role of ion drift in the ion deintercalation process, we used the equation $\frac{dc}{dt} = D\frac{d^2c}{dx^2}$ to fit the curve. The initial condition and boundary condition in $VO_2$ are set as follows: $c(x, t=0) = \begin{cases} 0 & x < -h \\ c_0 & -h < x < 0 \\ 0 & x > 0 \end{cases}$; total amount of indium is constant. Here $x < -h$ represents the $VO_2$ region, $-h < x < 0$ represents the $In_cVO_2$ region and $x > 0$ represents the

NaCl region, with diffusion occurring along the positive-$x$ direction. We assume $h = 20$ nm and $c_0 = 0.7\%$ based on Fig. 2h. The solution to the equation is as follows:

$$c(x,t) = \frac{c_0}{2}\left(\mathrm{erf}\left(\frac{x+h}{2\sqrt{Dt}}\right) - \mathrm{erf}\left(\frac{x}{2\sqrt{Dt}}\right)\right). \quad (4)$$

The diffusion of ions out of the $VO_2$ film, as described by equation (1), gradually restores the conductivity of $VO_2$. This phenomenon is not observed when the sample is simply immersed in DI water, suggesting that ion diffusion is more pronounced in diluted $H_2O_2$ solutions. To model the decrease in conductivity, we applied equation (4) to fit the conductivity and estimated deintercalation diffusivity $D$ to be $6 \times 10^{-13}$ cm$^2$ s$^{-1}$. The fitting results are shown in Supplementary Fig. 2. The diffusivity obtained from $H_2O_2$ treatment aligns closely with previous studies on the delithiation of $LiFePO_4$ in $H_2O_2$ solution, which reported values in the range of ~$10^{-14}$–$10^{-12}$ cm$^2$ s$^{-1}$ (ref. 35). These studies have highlighted that in the oxidation reactions, ion diffusion is not limited to the solid phase but also involves ion movement within the liquid phase, accounting for the higher diffusivity[35,36].

## Hydroxyl termination

**Hydroxyl groups at the metal oxide–water interface.** The formation and role of hydroxyl groups at the metal oxide–water interface were extensively discussed in earlier work[37]. Hydroxyl groups are formed by the dissociative chemisorption of water molecules, and these groups act as ion-exchange sites. Earlier studies[38] attributed surface hydroxyl groups to exposed lattice metal ions, which are strong Lewis acids that interact with oxygen in water. This led to the assumption that the surface hydroxyl group density would vary based on the type of metal ion. However, a later study[37] revealed that hydroxyl group densities are similar across many metal oxides. This finding attributes hydroxyl group formation predominantly to surface oxide ions, which are strong Lewis bases due to insufficient coordination with lattice metal ions. These surface oxide ions, characterized by larger size and low polarizing power, preferentially take up protons from water to form hydroxyl groups. This process dominates over contributions from lattice metal ions. From this study, the hydroxyl group densities for $TiO_2$ ($2.79 \times 10^{-5}$ mol m$^{-2}$) and $Cr_2O_3$ ($2.69 \times 10^{-5}$ mol m$^{-2}$) provide a reference for extrapolating the surface groups of $VO_2$.

Further research[39] into the hydrophilicity of metal oxide surfaces demonstrates that metal cations with higher electronegativity enable water molecules to form coordinate bonds with both metal and oxygen ions on the surface, resulting in a hydrophilic surface. Conversely, surfaces with lower-electronegativity metal ions tend to promote interactions in which water molecules bond exclusively with oxygen ions, resulting in a hydrophobic surface. Given that the electronegativity of vanadium lies between titanium and chromium, the hydrophilicity of $VO_2$ is anticipated to be comparable with those of $TiO_2$ and $Cr_2O_3$—both are hydrophilic in prior studies[40,41]. To confirm the hydrophilicity of $VO_2$, we measured the contact angles of DI water and 0.1-M NaCl solution on the $VO_2$ surface (Supplementary Fig. 6). The results demonstrate the hydrophilic behaviour in both cases, consistent with the conclusions from ref. 39.

**Hydroxyl groups at the metal oxide–NaCl interface.** Although specific studies on hydroxyl groups at the $VO_2$–NaCl solution interface are limited, relevant insights can be drawn from analogous systems. Ref. 42 discussed the $TiO_2$–NaCl interface, showing that the $TiO_2$ surface becomes hydroxylated when exposed to NaCl solutions. Additionally, the electric field at this interface is oriented towards the $TiO_2$ surface.

## Ionization of surface hydroxyl groups

Previous studies[37,43] have shown that hydroxyl groups at the solid–liquid interface can undergo protonation or deprotonation, leading to either absorption or release of protons. Surface hydroxyl groups are represented as –MOH, and protons near the surface are denoted with the subscript s. These reactions can be described as follows:

Protonation reaction: $-MOH + H_s^+ \leftrightarrow -MOH_2^+$
Deprotonation reaction: $-MOH \leftrightarrow -MO^- + H_s^+$

Ref. [42] illustrates that the surface of $TiO_2$ in a NaCl solution becomes negatively charged due to the dominance of the deprotonation reaction. As discussed in ref. 44, the protonation reaction results in a positively charged surface due to $H^+$ binding to surface groups, thereby reducing the free $H^+$ concentration in the solution and increasing the pH. Conversely, the deprotonation reaction leads to a negatively charged surface by releasing $H^+$ ions into the solution, increasing the free $H^+$ concentration and lowering the pH.

To characterize the dominant reaction for the $VO_2$ surface in NaCl solution, we measured the zeta potential. $VO_2$ nanoparticles (0.5 g) were dispersed in 500-ml NaCl solutions with concentrations of 0.01 M, 0.1 M and 1 M. For each dispersion, the pH of the NaCl solution decreased after the introduction of $VO_2$ nanoparticles. Initially, the pH values of the NaCl solutions were 6.8, 6.5 and 6.3 for 0.01 M, 0.1 M and 1 M concentrations, respectively. After adding $VO_2$ nanoparticles, the pH values dropped to 3.4, 3.2 and 3.1, respectively. This notable pH decrease indicates that additional $H^+$ ions were released into the solution, which corresponds to the dominance of the deprotonation reaction at the solid–liquid interface.

The zeta potential results (Supplementary Table 1) further support this conclusion. As noted in ref. 44, negative zeta potential values arise from surface hydroxyl group deprotonation. From Supplementary Table 1, we observe that all the measured zeta potentials are negative, indicating that the $VO_2$ surface carries a net negative charge. This observation aligns with the measured pH drop when $VO_2$ nanoparticles are suspended in the NaCl solution, confirming that deprotonation is the dominant surface reaction. Additionally, we find that as the NaCl concentration increases, the absolute value of the zeta potential also increases. It is noted that the relationship between zeta potential and solution concentration can vary, showing either a positive or negative correlation depending on the specific particle and solution type[45,46]. Previous studies have attributed a positive correlation to the shear plane moving closer to the solid surface at higher concentrations[46].

## Electric double layer analysis

From the discussion in the 'Hydroxyl termination' and 'Ionization of surface hydroxyl groups' sections, the surface of the $VO_2$ immersed in the NaCl solution carries negative charges, resulting in a corresponding charge redistribution in the solution[39,47]. In the NaCl solution, an IHP containing hydrogen ions dissociated from the water molecules is nearest to the solid surface. Following the IHP, an OHP consisting of cations exists. The IHP and OHP form the fixed layer that firmly adheres to the solid surface and is immobile. There is no net charge inside the IHP and OHP, where the electrical potential profile is linear; hence, the fixed layer can be described by the parallel-plate capacitor model. Beyond the OHP, there exists a diffuse layer with mobile ions, where the charges follow the Boltzmann distribution. The electrical potential decays exponentially within the diffuse layer.

The dominant deprotonation reaction at the $VO_2$ surface is expressed as

$$VOH \rightleftharpoons VO^- + H^+_{surface} \quad (5)$$

The presence of $VO^-$ groups at the $VO_2$ surface leads to a negatively charged surface and an electric field pointing towards $VO_2$.

## Estimation of surface pH

The surface pH was estimated using equation (6): $c_{H^+}(0) = c_{H^+}(\infty)\, e^{-|e|\varphi_0/k_B T}$. Here $c_{H^+}(\infty)$ represents the hydrogen ion concentration in the bulk solution, and $\varphi_0$ is the surface electrical potential.

The bulk pH of the 0.1-M NaCl solution was measured to be 6.5. Surface potential values were determined using the analytical model described in the 'Calculation model to estimate the surface electric field' section, where two coupled equations (equations (13) and (14)) were solved for the unknowns: the surface electric field $E$ and surface potential $\varphi_0$. In this model, the equilibrium constant pK of the surface reaction was determined to be 4.5 ± 0.9 through titration (Extended Data Fig. 6b–d). Assuming pK = 4.5, the estimated surface potential values are presented in Supplementary Fig. 8, showing that the surface potential at 0.1-M NaCl concentration is approximately −170 mV. The estimated surface potential (approximately −170 mV) and measured zeta potential (approximately −18 mV; Supplementary Table 1) are consistent with the reported values for the $TiO_2$–NaCl interface in the literature[42] (surface potential, approximately −138 mV; zeta potential, approximately −27 mV). Using this surface potential $\varphi_0$ in equation (6), the surface pH was estimated to be approximately 3.6. Considering the experimental uncertainty in pK (4.5 ± 0.9), the estimated surface pH range is 3.6 ± 0.5.

## Indium speciation at the solid–liquid interface

To elucidate indium speciation at the solid–liquid interface, we considered the Pourbaix diagram and potential hydrolysis reactions occurring at the surface.

Using The Materials Project[48], we generated the Pourbaix diagram for indium in NaCl solution (Extended Data Fig. 4). This diagram indicates that increasing the NaCl concentration from 0.01 M to 1 M has minimal impact on the distribution of soluble indium species. According to the Pourbaix diagram, a pH of 3.6 falls within the region of $In^{3+}$. This result is consistent with the hydrolysis analysis from previous studies[49,50], which indicate that at a pH of 3.6, the coexistent species include $In^{3+}$, $InOH^{2+}$ and $In(OH)_2^+$, with $In^{3+}$ being the most abundant. Within the pH range of 3.6 ± 0.5, indium species are still predominantly present as $In^{3+}$. In addition to concentration, steric energy penalties associated with $InOH^{2+}$ and $In(OH)_2^+$ make $In^{3+}$ the most favourable species for doping into the $VO_2$ surface.

## Analysis of ion proximity to $VO_2$ surface

In contrast to the substantial indium signals observed in $VO_2$ following exposure to NaCl, sodium signals were conspicuously absent (Extended Data Fig. 5b). To delve deeper into the surface composition, we utilized ARXPS. By increasing the sample angle, the depth range for ion detection within the sample is reduced, enabling ARXPS to capture signals from the ultrashallow surface within 10 nm (Extended Data Fig. 5c). The ARXPS results unveil that after immersion in a NaCl solution, the surface sodium signal became discernible. However, as the angle decreased, indicative of deeper layers in the sample bulk, the concentration of indium surpassed that of sodium rapidly (Extended Data Fig. 5d). These findings suggest that although a small quantity of sodium is doped into $VO_2$, it is confined primarily to the surface of $VO_2$, whereas indium exhibits a capacity to penetrate much deeper into the bulk of $VO_2$.

Together with the findings in Fig. 2e,f, the results suggest that ions within the OHP are more likely to be driven into the $VO_2$ film due to the strong surface electric field, whereas ions outside the OHP experience a notably reduced electric field, reducing the likelihood of being pushed into the film. With indium metal directly attached to the $VO_2$ surface, numerous indium ions are generated within the OHP and efficiently driven into $VO_2$. The majority of sodium ions remain in the diffuse layer and the solution body, and have a lower probability of penetrating the OHP, resulting in a much smaller amount of sodium ions being doped at the top surface of $VO_2$. When $VO_2$ is immersed alone in a NaCl/$In^{3+}$ solution, most indium ions also exist outside the OHP, leading to a much lower level of indium doping in $VO_2$. In the case of In/Au/$VO_2$, since the fixed layer is only a few nanometres thick[51], the 100-nm gold layer effectively blocks most of the generated indium ions from entering the OHP, making it challenging for indium to be driven into $VO_2$.

In the $VO_2$ plane, areas closer to indium metal exhibit higher doping levels, whereas areas farther from indium metal still show some level of doping. Since indium ions outside the Debye length can hardly approach the $VO_2$ surface, substantial ion diffusion occurs along the $VO_2$–liquid interface within the Debye length. This in-plane ion diffusion at the solid–liquid interface is consistent with the findings reported before[52], where fast lithium ion diffusion was observed at the $Li_xFePO_4$–electrolyte interface. This fast in-plane diffusion was attributed to lithium ions not needing to cross the double layer or undergo charge transfer, and this conclusion aligns with our observations.

## Calculation model to estimate the surface electric field

In a scenario in which the electric potential in the bulk solution is 0, the proton concentration at the surface $c_{H^+}(0)$ is given by

$$c_{H^+}(0) = c_{H^+}(\infty)\, e^{-|e|\varphi_0/k_B T} \tag{6}$$

Here $c_{H^+}(\infty)$ represents the proton concentration in the bulk solution, $|e|$ is the elementary charge, $\varphi_0$ is the electric potential on the surface ($\varphi_0 < 0$), $k_B$ is the Boltzmann constant and $T$ is the temperature. The equilibrium constant ($K$) from equation (6) is expressed as

$$K = \frac{C_{H^+}(0) \cdot \Gamma_{VO^-}}{\Gamma_{VOH}}, \tag{7}$$

where $\Gamma_{VO^-}$ and $\Gamma_{VOH}$ are site densities of $VO^-$ and VOH at the $VO_2$ surface, respectively. Thus, the charge density $\sigma$ of the $VO_2$ surface is given by

$$\sigma(\varphi_0) = -|e|\,\Gamma_{VO^-} = \frac{-|e|\,K \cdot \Gamma_{VOH}}{10^{-pH}} e^{|e|\varphi_0/k_B T}. \tag{8}$$

We assumed the validity of the Boltzmann distribution across both diffuse layer and fixed layer[53]. Considering the higher concentration of electrolytic ions compared with $H^+$ and $OH^-$, the electric potential is determined by the distribution of electrolytic ions. The concentration $c_i$ of electrolytic ion $i$ is given by

$$c_i(x) = c_{i\infty} e^{-z_i|e|\varphi(x)/k_B T}. \tag{9}$$

Here $z_i$ is the charge number of ion $i$ (positive for $Na^+$ and negative for $Cl^-$), and $c_{i\infty}$ is the concentration of ion $i$ in the bulk solution. According to the Poisson–Boltzmann equation, we have

$$\begin{aligned}\frac{d^2\varphi(x)}{dx^2} &= -\frac{\rho}{\varepsilon_l} = -\frac{|e|\,c_{NaCl}}{\varepsilon_l}\left[e^{-|e|\varphi(x)/k_B T} - e^{|e|\varphi(x)/k_B T}\right] \\ &= \frac{2|e|c_{NaCl}}{\varepsilon_l}\sinh\frac{|e|\,\varphi(x)}{k_B T}.\end{aligned} \tag{10}$$

Here $\varepsilon_l$ is the dielectric constant of the solution and $c_{NaCl}$ is the NaCl concentration. Equation (10) is solved by noting that $\frac{d^2\varphi(x)}{dx^2} = \frac{1}{2}\frac{d}{d\varphi}\left(\frac{d\varphi}{dx}\right)^2$, with the boundary conditions $\varphi(\infty) = 0$ and $\left.\frac{d\varphi(x)}{dx}\right|_{x=\infty} = 0$, and equation (11) is obtained:

$$\frac{d\varphi}{dx} = -\sqrt{\frac{8c_{NaCl}k_B T}{\varepsilon_l}}\sinh\frac{|e|\,\varphi}{2k_B T}. \tag{11}$$

Defining the Debye screening length as $L_D = \sqrt{\frac{\varepsilon_l k_B T}{2e^2 c_{NaCl}}}$, equation (11) becomes

$$\frac{d\varphi}{dx} = -\frac{2k_B T/|e|}{L_D}\sinh\frac{|e|\,\varphi}{2k_B T}. \tag{12}$$

The electric field at the solid–liquid interface can be determined by combining equation (8) with Gauss's law:

$$E(\varphi_0) = \left|\frac{\sigma(\varphi_0)}{\varepsilon_l}\right| = \frac{|e|K \cdot \Gamma_{VOH}}{\varepsilon_l \cdot 10^{-pH}} e^{|e|\varphi_0/k_BT}. \quad (13)$$

From equation (12), the strength of the surface electric field is given by

$$E(\varphi_0) = \left|-\frac{d\varphi}{dx}\Big|_{x=0}\right| = -\frac{2k_BT/|e|}{L_D} \sinh\frac{|e|\varphi_0}{2k_BT} (\varphi_0 < 0). \quad (14)$$

Combining equations (13) and (14), the relationship between electric field and electrolyte concentration is obtained by setting $e^{|e|\varphi_0/2k_BT} = \sqrt{\alpha E}$, where $\alpha = \frac{\varepsilon_s \cdot 10^{-pH}}{|e|K \cdot \Gamma_{VOH}}$. This simplifies equation (14) to $E = -\frac{2k_BT/|e|}{L_D} \sinh\frac{|e\varphi_0|}{2k_BT} = \frac{k_BT}{|e|L_D}(\frac{1}{\sqrt{\alpha E}} - \sqrt{\alpha E})$. Thus, the electric field is the solution of $\frac{|e|L_D}{k_BT}E = \frac{1}{\sqrt{\alpha E}} - \sqrt{\alpha E}$. In Extended Data Fig. 6a, a higher concentration leads to a smaller Debye screening length $L_D$, resulting in a higher electric field $E$. If the electrolyte concentration is very high, the electric field approaches $E_{max} = 1/\alpha$. For a very low concentration, $\frac{|e|L_D}{k_BT}E = \frac{1}{\sqrt{\alpha E}}$ and $E(c_{NaCl}) \propto [\frac{2k_BTc_{NaCl}}{\varepsilon_l\alpha}]^{\frac{1}{3}} \propto c_{NaCl}^{1/3}$. The results are shown in Fig. 2g.

To determine the surface electric-field value, titration experiments were conducted to obtain the equilibrium constant K. The resulting titration curves were analysed using ProtoFit (v. 2.1) software[54]. Within the software, $Q_{ads}$ denotes the protons exchanged with the adsorbent, that is, $VO_2$ powder. $Q^*_{ads}$ represents the derivative function of $Q_{ads}$ with respect to the pH value, making it a more sensitive indicator for evaluating the fitting. By fitting $Q^*_{ads}$, the pK ($-\log_{10}$[K]) value is estimated to be 4.5 ± 0.9 (Extended Data Fig. 6b–d), and the range of the pK value is close to the other estimated values in $TiO_2$ (ref. 55). $\Gamma_{VOH}$ is estimated to be 8 $nm^{-2}$ (ref. 47). With these parameters, the surface electric field is calculated and summarized in Supplementary Table 2.

## Fitting depth profile of indium in $VO_2$

Fick's second law of diffusion is given by $\frac{dc}{dt} = D\frac{d^2c}{dx^2}$. The initial condition is set as $c(x, t=0) = \phi(x) = \begin{cases} c_0 & x = 0 \\ 0 & x > 0 \end{cases}$, and the boundary condition is set as $c(x=0, t) = c_0$. In this setup, $x > 0$ represents the $VO_2$ region, and $x < 0$ represents the NaCl region, with diffusion occurring along the positive-$x$ direction. The resultant solution is given by

$$c(x,t) = c_0\left[1 - \mathrm{erf}\left(\frac{x}{2\sqrt{Dt}}\right)\right]. \quad (15)$$

The diffusivity of indium ($D$) in $VO_2$ was determined to be approximately $6 \times 10^{-17}$ $cm^2$ $s^{-1}$ by fitting the depth profile as shown in Fig. 2h.

## Fitting conductivity data following NaCl treatment with diffusion and drift

To accurately fit the conductivity curves, we initially assumed a surface electric field that exponentially decays with depth, represented as $E = E_0e^{-x/x_0}$. Here $x_0$ denotes the penetration depth of the electric field, estimated to be 20 nm. Using numerical methods and constant-concentration boundary condition, we successfully achieved a good fit for conductivity (Supplementary Fig. 10a). Moreover, considering that the drift flux notably exceeds the diffusion flux (Supplementary Fig. 10b,c), it is reasonable to presume that the surface electric field remains constant. Consequently, we simplified the problem by assuming a constant electric field. Using Fourier transform, we derived the analytical solution:

$$c(x,t) = c_0\left[1 - \mathrm{erf}\left(\frac{x - \mu Et}{2\sqrt{Dt}}\right)\right]. \quad (16)$$

In equation (16), the indium mobility in $VO_2$ is estimated using the Einstein relation, $\mu = \frac{Dq}{k_BT}$, where $D$ is estimated in the 'Fitting depth profile of indium in $VO_2$' section. This results in $\mu \approx 10^{-15}$ $cm^2$ $V^{-1}$ $s^{-1}$. By fitting the conductivity data in Fig. 1c, the extracted surface electric fields are presented in Supplementary Table 2, demonstrating consistency with the calculated surface electric fields. When we simultaneously adjust the diffusivity and electric field and maintain a coefficient of determination of $R^2 \geq 0.95$, the diffusivity was on the order of $10^{-17}$ $cm^2$ $s^{-1}$, consistent with the data extracted from Fig. 2h.

## Second approach to fit conductivity data—constant-flux boundary condition

A constant-concentration boundary condition was initially used, as sufficient $In^{3+}$ ions are present within the Debye layer (Extended Data Fig. 7). To further evaluate the interfacial kinetics, a constant-flux boundary condition was also applied as a different approach.

Direct contact with indium metal leads to a high concentration of $In^{3+}$ near the $VO_2$ surface. As a result, mass transport to the interface is efficient, and the rate-limiting step is the interfacial hopping of ions from the liquid to the solid $VO_2$ side. The flux is written as $J = r_{hop}\sigma_{In}$, where $\sigma_{In}$ is the surface density of indium ions and can be seen as a constant. Prior studies[56] have shown that electric fields can notably enhance the hopping rate $r_{hop}$.

To implement the constant-flux boundary condition, the indium ion concentration $c$ at the boundary is updated at each time step to satisfy a constant injection flux $J_{in} = \mu Ec - D\frac{\partial c}{\partial x}$. The applied flux value and simulation results are shown in Supplementary Fig. 11.

## DFT calculations

First-principles defect calculations and electronic structure analysis were performed in the plane-wave basis using Vienna ab initio simulation package (v. 5.4.4)[57–59]. Exchange–correlation interactions were treated with the generalized gradient approximation using the Perdew–Burke–Ernzerhof functional[60,61]. Hubbard $U$ corrections were applied to the vanadium 3$d$ electrons, using the formulation in ref. 62, with a value of $U - J = 3.0$ eV selected based on the reported benchmarks for M1 $VO_2$ and our own tests on the bandgap of bulk $VO_2$ crystal[63,64]. The projector-augmented wave formalism with Perdew–Burke–Ernzerhof/generalized gradient approximation potential files labelled 'V_pv'; 'O'; and 'In_d' were used to incorporate the 4$s$, 3$d$ and 3$p$ states for vanadium; the 2$s$ and 2$p$ states for oxygen; and the 4$d$, 5$s$ and 5$p$ states for indium, as the valence orbitals[61], respectively. The simulation supercell for bulk $VO_2$ was constructed by replicating the M1 $VO_2$ unit cell in a $2 \times 2 \times 2$ arrangement, yielding a total of 96 atoms in the non-defected system. All calculations utilized a plane-wave energy cut-off of 600 eV and Gaussian smearing methods with a width of 0.03 eV. Structural relaxations and energy calculations were performed using a Γ-centred $3 \times 3 \times 3$ $k$-point mesh and an energy convergence threshold of $5 \times 10^{-5}$ eV. Calculations for electronic properties such as bandgap and projected density of states were performed with a finer $7 \times 7 \times 7$ $k$-point mesh and an energy convergence criterion of $1 \times 10^{-6}$ eV.

Spin polarization was included in all the calculations to model the magnetic contributions to defect energies and transition levels. To reproducibly achieve the most energetically stable magnetic ground state, we evaluated the diamagnetic, ferromagnetic and antiferromagnetic configurations for pristine M1 $VO_2$. Our results indicate that an antiferromagnetic configuration characterized by an alternating up–down (udud) magnetic-moment distribution, in which each vanadium atom carries an approximately 1-Bohr magneton, yields the lowest total energy. This finding is consistent with previous DFT studies on the electronic and magnetic properties of bulk $VO_2$ (M)[64]. Accordingly, this configuration was used as the initial guess for local magnetization in all structural relaxations. For defect calculations in which the additional charge was introduced, several initial magnetization assignments were considered (with the additional charge either delocalized, localized near or separated away from the defect core), and the configuration converging to the lowest total energy was adopted as the ground state[65].

### Calculation of defect formation energies

Kröger–Vink point defect notation is used to identify the defect type and charge state throughout this study. The formation energy of defects in charge state $q$ was calculated using the dilute-limit, grand-canonical formalism[66]:

$$E_D^f = E[\text{defect}] - E[\text{pristine}] + \sum_i n_i\mu_i + q(E_F + E_{VBM}) + E_{corr}, \quad (17)$$

where $E$[defect] and $E$[pristine] denote the total energies of the defect-containing and pristine supercells, respectively. The term $\sum_i n_i\mu_i$ accounts for the chemical potential contribution from the addition or removal of $n_i$ particles and $E_F$ denotes the Fermi level referenced to the valence band maximum $E_{VBM}$. $E_{corr}$ is the finite-size correction for artefacts arising from the electrostatic interaction of image charges due to periodic boundary conditions[67]. To evaluate $E_{corr}$ in $VO_2$, we used the Freysoldt–Neugebauer–Van de Walle scheme, as generalized by Kumagai and Oba, and implemented in the Spinney package[67–69]. This a posteriori correction aligns the electrostatic potentials between the bulk and defected supercells using atomic site potentials, with the required static dielectric tensor elements obtained via density functional perturbation theory calculations in the Vienna ab initio simulation package[70].

Formation enthalpies of all relevant species were calculated using the generalized gradient approximation/Perdew–Burke–Ernzerhof + $U$ functional, without a posteriori adjustments from experimental or thermally corrected data. It should be noted that the oxygen reference energy in this work was determined from the total energy of oxygen molecules in a spin-polarized state[71]. The chemical potentials of oxygen and vanadium are constrained by the equilibrium boundary condition $\mu_V + 2\mu_O = \mu_{VO_2}$, where $\mu_{VO_2}$ is the computed total energy of the pristine $VO_2$ crystal. This condition can be reformulated as

$$\Delta H_f^{VO_2} = (\mu_V - \mu_V^0) + 2(\mu_O - \mu_O^0) = \Delta\mu(V) + 2\Delta\mu(O), \quad (18)$$

where $\mu_V^0$ and $\mu_O^0$ denotes the energies per atom of metallic vanadium and ferromagnetic oxygen reference states, respectively. $\Delta H_f^{VO_2}$ is the DFT-calculated formation enthalpy of $VO_2$ with respect to its elemental constituents. $\Delta\mu$(V) and $\Delta\mu$(O) represent changes in vanadium and oxygen chemical potentials due to different environmental conditions, respectively. Experimental evidence from XPS shows a reduction in the vanadium oxidation state from +4 to a mixed +4/+3 configuration, whereas TEM imaging confirms the preservation of the $VO_2$ lattice structure during the electronic transition. These findings indicate that $VO_2$ undergoes reduction without the formation of alternative oxide phases, thereby supporting the application of reducing limit chemical potentials in defect formation calculations. To best represent the reducing environment in experimental settings, $\mu_O$ and $\mu_V$ were set to the zero-temperature stability limit of $VO_2$, where bulk $VO_2$ is in thermodynamic equilibrium with the adjacent phase $V_3O_5$, whose formation enthalpy is defined as

$$3\Delta\mu(V) + 5\Delta\mu(O) = \Delta H_d^{V_3O_5}, \quad (19)$$

which, when solved concurrently with energy conservation relation outlined in equation (18), yields $\Delta\mu$(O) = −1.586 eV and $\Delta\mu$(V) = −1.373 eV. In the experimental setup, since metallic indium in direct contact with the $VO_2$ thin film serves as the exclusive reservoir for indium ions, the indium chemical potential in equilibrium with $VO_2$ under reducing conditions could be determined by imposing a stability constraint that favours metallic indium over its oxide. Accordingly, $\Delta\mu$(In) is calculated by combining In–$In_2O_3$ equilibrium boundary condition with the previously determined oxygen energy:

$$2\Delta\mu(In) + 3\Delta\mu(O) \geq \Delta H_f^{In_2O_3} \Rightarrow \Delta\mu(In) = -1.628\ \text{eV}.$$

Finally, the chemical potential of the solvated sodium cations in the 0.1-M NaCl solution used in the experiment was determined from the reported sodium standard electrode potential, incorporating a concentration correction via the Nernst equation for ideal solutions[72]:

$$\mu(Na^+, 0.1\,M) = \mu^0(Na^+, 1\,M) + k_B T \ln[0.1],$$

$$\Delta\mu(Na^+) = \mu(Na^+) - \mu_{Na}^0 = -1.456\ \text{eV}.$$

Formation energies for the two intrinsic ($vac_O$, $vac_V$) and three extrinsic ($Na_{int}$, $In_{int}$, $In_V$) defects in $VO_2$ under reducing conditions were then evaluated using the above derived chemical potentials and equation (17). When the Fermi level is set at the valence band maximum, indium doping exhibits the lowest $E_D^f$ among all defects. The charged defect formation phase diagram (Fig. 2b) was constructed by plotting $E_D^f$ as a function of the Fermi level, with only the lowest-energy charge states displayed for clarity.

## Data availability

All relevant data that support the findings of this study are available via Zenodo at https://doi.org/10.5281/zenodo.15758758 (ref. 73). Source data are provided with this paper.

## References


31. Qiao, R. et al. High-efficiency in situ resonant inelastic X-ray scattering (iRIXS) endstation at the Advanced Light Source. *Rev. Sci. Instrum.* **88**, 033106 (2017).
32. Kurmaev, E. Z. et al. Oxygen X-ray emission and absorption spectra as a probe of the electronic structure of strongly correlated oxides. *Phys. Rev. B* **77**, 165127 (2008).
33. Stępień, J., Sikora, M., Kapusta, C., Pomykalska, D. & Bućko, M. M. Determination of oxygen vacancy limit in Mn substituted yttria stabilized zirconia. *J. Appl. Phys.* **123**, 185108 (2018).
34. Hazarika, R. & Kalita, B. Effect of oxygen vacancy defects on electronic and optical properties of MgO monolayers: first principles study. *Mater. Sci. Eng. B* **286**, 115974 (2022).
35. Kurbatov, A. P. et al. Chemical oxidation of $LiFePO_4$ in aqueous medium as a method for studying kinetics of delithiation. *Russ. J. Electrochem.* **54**, 225–233 (2018).
36. Weichert, K. et al. Phase boundary propagation in large $LiFePO_4$ single crystals on delithiation. *J. Am. Chem. Soc.* **134**, 2988–2992 (2012).
37. Tamura, H., Mita, K., Tanaka, A. & Ito, M. Mechanism of hydroxylation of metal oxide surfaces. *J. Colloid Interface Sci.* **243**, 202–207 (2001).
38. Anderson, M. & Rubin, A. Adsorption of inorganics at solid-liquid interfaces. *Soil Sci.* **133**, 257–258 (1982).
39. Zenkin, S., Kos, Š. & Musil, J. Hydrophobicity of thin films of compounds of low-electronegativity metals. *J. Am. Ceram. Soc.* **97**, 2713–2717 (2014).
40. Xi, Y., Qi, Y., Mao, Z., Yang, Z. & Zhang, J. Surface hydrophobic modification of $TiO_2$ and its application to preparing PMMA/$TiO_2$ composite cool material with improved hydrophobicity and anti-icing property. *Constr. Build. Mater.* **266**, 120916 (2021).
41. Luo, S., Huo, J. C., Lei, H. & Deng, J. Study of the hydrophobic modification of chromium sesquioxide with lauric acid. *Adv. Mater. Res.* **535–537**, 1586–1590 (2012).
42. Bischoff, M., Biriukov, D., Předota, M., Roke, S. & Marchioro, A. Surface potential and interfacial water order at the amorphous $TiO_2$ nanoparticle/aqueous interface. *J. Phys. Chem. C* **124**, 10961–10974 (2020).

43. Lützenkirchen, J. Comparison of 1-pK and 2-pK versions of surface complexation theory by the goodness of fit in describing surface charge data of (hydr)oxides. *Environ. Sci. Technol.* **32**, 3149–3154 (1998).
44. Li, M. et al. Relationship between surface hydroxyl complexation and equi-acidity point pH of $MnO_2$ and its adsorption for $Co^{2+}$ and $Ni^{2+}$. *ACS Omega* **7**, 9602–9613 (2022).
45. Kitagawa, Y., Yamaguchi, S. & Yorozu, Y. Effects of sodium chloride concentrations on zeta potentials of clay minerals estimated by an electrokinetic sonic amplitude method. *Clay Sci.* **12**, 91–96 (2003).
46. Vilasau, J. et al. Stability of oil-in-water paraffin emulsions prepared in a mixed ionic/nonionic surfactant system. *Colloids Surf. A Physicochem. Eng. Asp.* **389**, 222–229 (2011).
47. Behrens, S. H. & Grier, D. G. The charge of glass and silica surfaces. *J. Chem. Phys.* **115**, 6716–6721 (2001).
48. Jain, A. et al. Commentary: The Materials Project: a materials genome approach to accelerating materials innovation. *APL Mater.* **1**, 011002 (2013).
49. Kluczka, J. A review on the recovery and separation of gallium and indium from waste. *Resources* **13**, 35 (2024).
50. Baes, C. F. & Mesmer, R. S. The hydrolysis of cations. *Ber. Bunsenges. Phys. Chem.* **81**, 245–246 (1977).
51. Brown, M. A., Goel, A. & Abbas, Z. Effect of electrolyte concentration on the Stern layer thickness at a charged interface. *Angew. Chem. Int. Ed.* **55**, 3790–3794 (2016).
52. Li, Y. et al. Fluid-enhanced surface diffusion controls intraparticle phase transformations. *Nat. Mater.* **17**, 915–922 (2018).
53. Bard, A. J. & Faulkner, L. R. *Electrochemical Methods: Fundamentals and Applications* (Wiley, 2001).
54. Turner, B. F. & Fein, J. B. Protofit: a program for determining surface protonation constants from titration data. *Comput. Geosci.* **32**, 1344–1356 (2006).
55. Piasecki, W. 1pK and 2pK protonation models in the theoretical description of simple ion adsorption at the oxide/electrolyte interface: a comparative study of the predicted and observed enthalpic effects accompanying adsorption of simple ions. *Langmuir* **18**, 4809–4818 (2002).
56. Schmickler, W. & Santos, E. in *Interfacial Electrochemistry* (eds Schmickler, W. & Santos, E.) 177–193 (Springer, 2010).
57. Kresse, G. & Hafner, J. Ab initio molecular dynamics for liquid metals. *Phys. Rev. B* **47**, 558–561 (1993).
58. Kresse, G. & Furthmüller, J. Efficiency of ab-initio total energy calculations for metals and semiconductors using a plane-wave basis set. *Comput. Mater. Sci.* **6**, 15–50 (1996).
59. Kresse, G. & Furthmüller, J. Efficient iterative schemes for ab initio total-energy calculations using a plane-wave basis set. *Phys. Rev. B* **54**, 11169–11186 (1996).
60. Perdew, J. P., Burke, K. & Ernzerhof, M. Generalized gradient approximation made simple. *Phys. Rev. Lett.* **77**, 3865–3868 (1996).
61. Kresse, G. & Joubert, D. From ultrasoft pseudopotentials to the projector augmented-wave method. *Phys. Rev. B* **59**, 1758–1775 (1999).
62. Dudarev, S. L., Botton, G. A., Savrasov, S. Y., Humphreys, C. J. & Sutton, A. P. Electron-energy-loss spectra and the structural stability of nickel oxide: an LSDA+*U* study. *Phys. Rev. B* **57**, 1505–1509 (1998).
63. Kylänpää, I. et al. Accuracy of ab initio electron correlation and electron densities in vanadium dioxide. *Phys. Rev. Mater.* **1**, 065408 (2017).
64. Stahl, B. & Bredow, T. Critical assessment of the DFT+*U* approach for the prediction of vanadium dioxide properties. *J. Comput. Chem.* **41**, 258–265 (2020).
65. Srivastava, S., Uberuaga, B. P. & Asta, M. Density functional theory study of local environment effects on oxygen vacancy properties in magnetite. *J. Phys. Chem. C* **127**, 17460–17472 (2023).
66. Freysoldt, C. et al. First-principles calculations for point defects in solids. *Rev. Mod. Phys.* **86**, 253–305 (2014).
67. Freysoldt, C., Neugebauer, J. & Van De Walle, C. G. Fully ab initio finite-size corrections for charged-defect supercell calculations. *Phys. Rev. Lett.* **102**, 016402 (2009).
68. Freysoldt, C., Neugebauer, J. & Van De Walle, C. G. Electrostatic interactions between charged defects in supercells. *Phys. Status Solidi B* **248**, 1067–1076 (2011).
69. Kumagai, Y. & Oba, F. Electrostatics-based finite-size corrections for first-principles point defect calculations. *Phys. Rev. B* **89**, 195205 (2014).
70. Gonze, X. & Lee, C. Dynamical matrices, Born effective charges, dielectric permittivity tensors, and interatomic force constants from density-functional perturbation theory. *Phys. Rev. B* **55**, 10355–10368 (1997).
71. Liu, B., Xiao, H., Zhang, Y., Aidhy, D. S. & Weber, W. J. Investigation of oxygen point defects in cubic $ZrO_2$ by density functional theory. *Comput. Mater. Sci.* **92**, 22–27 (2014).
72. Bratsch, S. G. Standard electrode potentials and temperature coefficients in water at 298.15 K. *J. Phys. Chem. Ref. Data* **18**, 1–21 (1989).
73. Guo, R. Data for 'Mem-sensing by surface ion migration within Debye length'. *Zenodo* https://doi.org/10.5281/zenodo.15758758 (2025).


## Acknowledgements

We are grateful for helpful discussions with D. E. Feldman, M. Shapira and K. Ashrafi. This work is supported by the US Department of Energy, Office of Science, Office of Basic Energy Sciences, Materials Sciences and Engineering Division, under contract no. DE-AC02-05CH11231 (Electronic Materials program, to J. Wu). This work made use of the computational resources provided at the Pittsburgh Supercomputing Center (PSC) Bridges-2 through allocation no. TG-DMR110087 from the Advanced Cyberinfrastructure Coordination Ecosystem: Services and Support (ACCESS) program, which is supported by National Science Foundation grant nos. 2138259, 2138286, 2138307, 2137603 and 2138296 (to M.A.). M.A. thanks the US Department of Energy, Office of Science, Office of Basic Energy Sciences, Materials Sciences and Engineering Division, under contract no. DE-AC02-05CH11231 within the Materials Project program (KC23MP), for supervision of the computation work related to point defects. Soft X-ray spectroscopy and data processing used resources of the Advanced Light Source, which is a Department of Energy, Office of Science User Facility, under contract no. DE-AC02-05CH11231 (to W.Y.). Work at the Molecular Foundry was supported by the US Department of Energy, Office of Science, Office of Basic Energy Sciences, under contract no. DE-AC02-05CH11231 (to K.C.B.). We thank the US Department of Energy, Office of Science, Office of Basic Energy Sciences, Materials Sciences and Engineering Division, under contract no. DE-AC02-05CH11231 within the KCWF16 program (to F.W.); the US Department of Energy, Office of Science, Office of Basic Energy Sciences, Materials Sciences and Engineering Division, under contract no. DE-AC02-05CH11231 within the KC22ZH program (to H.Z.); National Key R&D Program of China 2022YFB4400300; National Natural Science Foundation of China (62274003, 61927901 and 92164203; to K.T.); Key R&D Program of China grant no. 2023YFB3208700; National Natural Science Foundation of China grant no. 62375151; and Start-up funding in Tsinghua Shenzhen International Graduate School, Tsinghua University (to K.D.).

## Author contributions

J. Wu, K.T. and R.G. conceptualized this project. J. Wu supervised the work. R.G. performed the overall experiments. J. Wu and R.G.

derived the calculation model to estimate the surface electric field. R.G. carried out the analytical solution of the diffusion-related partial differential equations, with input from J. Wu and Q.F. R.G. performed the numerical simulations to fit the conductivity data. R.G., K.T., L.S. and J. Wu designed the biomimicry experiments. R.G., Q.F. and D.S.R. implemented the biomimicry experiments. R.G. and Q.F. contributed to the electrical measurements. F.W. is the PI of Q.F. K.M. conducted the DFT calculations. M.A. is the co-PI of K.M. and PI of the computational resources allocations. M. Sherburne is the co-PI of K.M. G.-H.L. and W.Y. performed the XAS and XES characterizations and analysed the data. M.J. conducted the FIB experiments. M.J. and K.C.B. conducted TEM on the FIB samples. M. Scott is the PI of M.J. R.G. and X.Z. performed the XPS characterizations. R.G. and Q.F. analysed the XPS data. M. Salmeron is the PI of X.Z. J. Wan performed the TEM characterization under the supervision of H.Z. R.G. and Q.F. analysed the TEM results. R.G., Yuhang Cai and J.S. prepared the $VO_2$ films. R.G. and J.S. conducted the titration experiments. R.G. and Q.F. prepared the responses to the reviewers, under the supervision of J. Wu and K.T. R.G., Q.F. and K.M. prepared the figures. All authors revised the paper.

## Competing interests

The authors declare no competing interests.

## Additional information

**Extended data** is available for this paper at https://doi.org/10.1038/s41563-025-02312-9.

**Supplementary information** The online version contains supplementary material available at https://doi.org/10.1038/s41563-025-02312-9.

**Correspondence and requests for materials** should be addressed to Kechao Tang or Junqiao Wu.

**Peer review information** *Nature Materials* thanks Sarbajit Banerjee, Paul Robin and Yoeri van de Burgt for their contribution to the peer review of this work.

https://doi.org/10.1038/s41563-025-02312-9

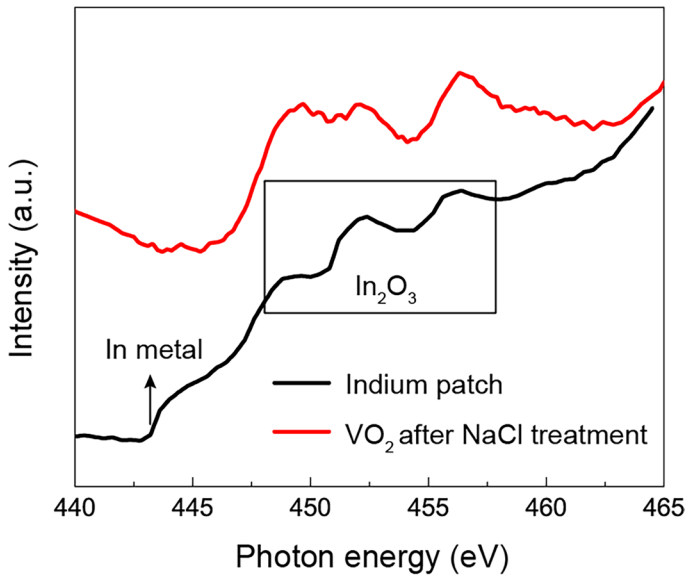


**Extended Data Fig. 1 | XAS results of indium M edge.** Black: detection on the indium patch on the $VO_2$ film. Red: measurement on $VO_2$ sample after NaCl treatment (separated from the indium patch).

https://doi.org/10.1038/s41563-025-02312-9

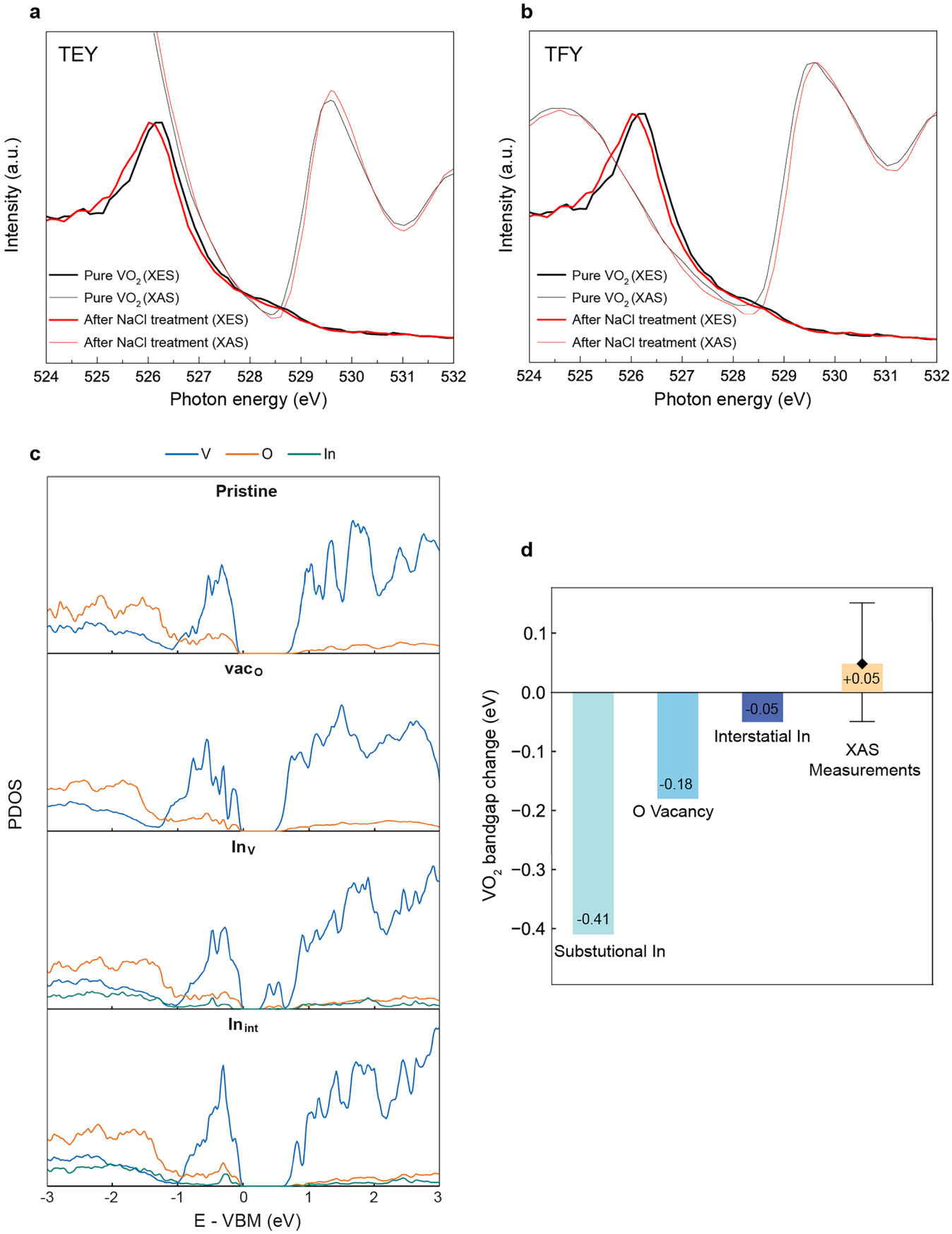


**Extended Data Fig. 2 | See next page for caption.**

https://doi.org/10.1038/s41563-025-02312-9

**Extended Data Fig. 2 | Electronic structure analysis of defect types in $VO_2$ via XAS/XES and DFT Calculations. a**, XES (thick lines) and total electron yield of XAS (thin lines). **b**, XES (thick lines) and total fluorescence yield of XAS (thin lines). Black: pure (pristine) $VO_2$. Red: $VO_2$ after treatment with 0.1 M NaCl solution for 5 min. **c**, DFT calculated projected density of states (PDOS) for pristine M1 $VO_2$, $VO_2$ with oxygen vacancy, $VO_2$ with indium substituting the vanadium site, and $VO_2$ with indium at the octahedral interstitial site. The horizontal axis indicates energy relative to the valence band maximum (VBM) for each system. **d**, Comparison of DFT-computed bandgap changes in $VO_2$ for various point defects at high concentrations with experimental bandgap estimates derived from XAS measurements. The bandgap change from experiments was estimated from the shift in the onset of TEY XAS spectra before and after NaCl soaking. One data point (n = 1) is presented as 0.05 eV with an error bar of ±0.1 eV, reflecting the instrument resolution of 0.2 eV.

https://doi.org/10.1038/s41563-025-02312-9

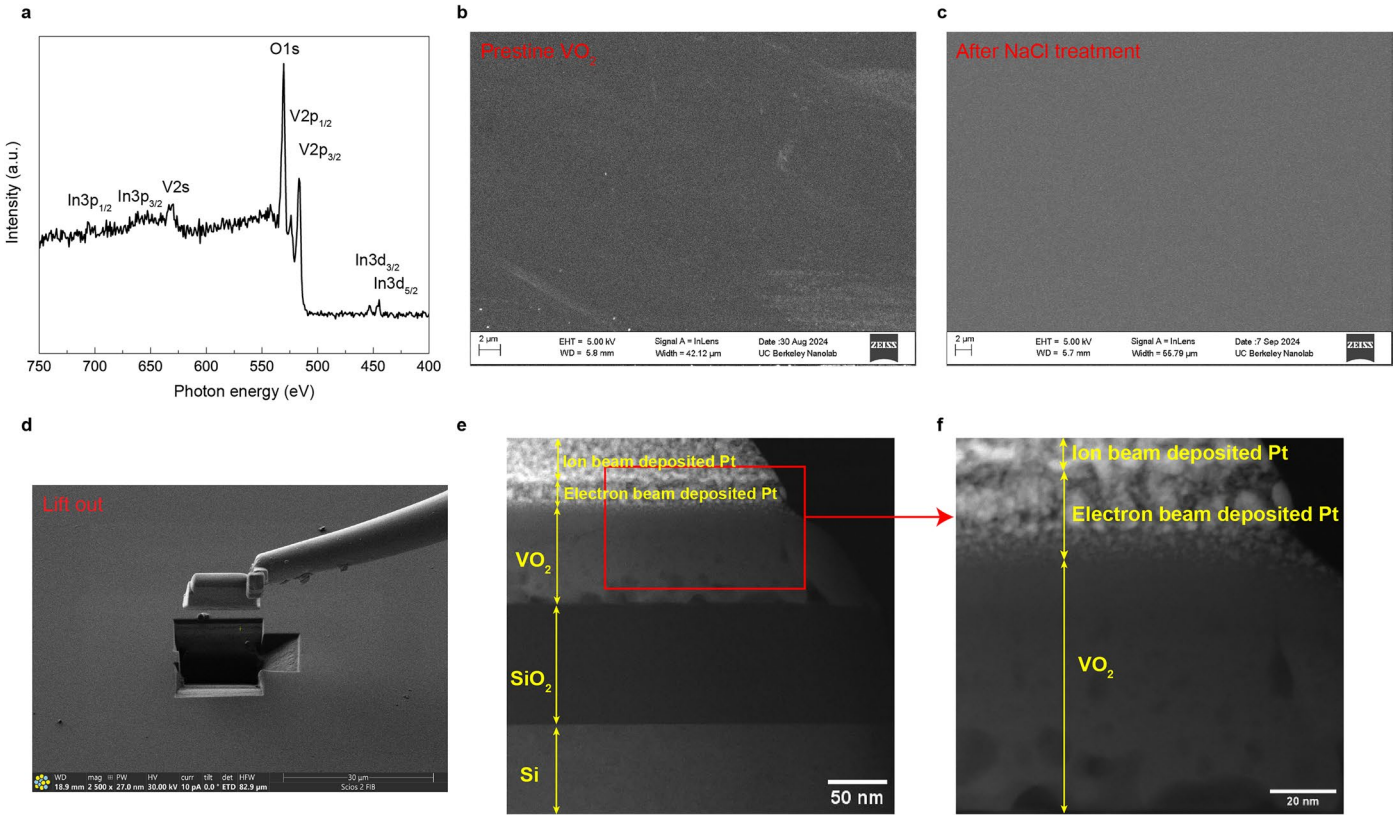


**Extended Data Fig. 3 | XPS, SEM, and FIB-TEM analysis of $VO_2$.** **a**, XPS spectrum of a clean $VO_2$ region after soaking in NaCl solution, confirming the presence of indium signal. **b**–**f**, SEM and FIB-TEM images confirm the absence of precipitates on the $VO_2$ surface following NaCl treatment. **b**, SEM image of pristine $VO_2$. **c**, SEM image of $VO_2$ sample analyzed in (**a**), showing no evidence of surface precipitates. **d**, SEM image during the FIB lift-out process. **e**, TEM cross-sectional image of the lift-out sample. A protective layer of electron-beam deposited Pt and ion beam deposited Pt covers the $VO_2$ surface. **f**, Magnified view of the red box in (**e**), revealing no indium precipitation on the $VO_2$ surface.

https://doi.org/10.1038/s41563-025-02312-9

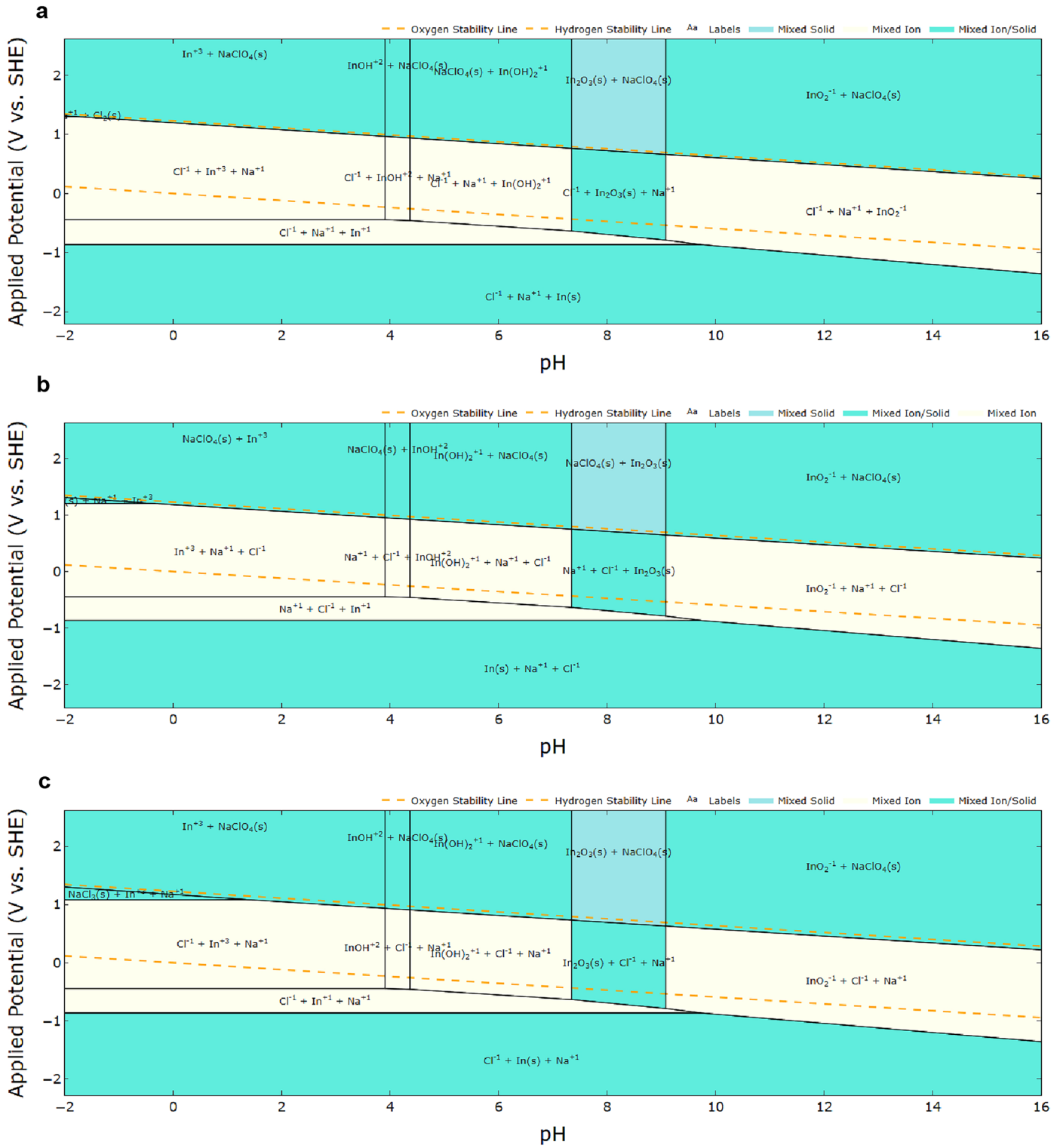


**Extended Data Fig. 4 | Pourbaix diagram of indium in NaCl solution. a**, 0.01 M NaCl. **b**, 0.1 M NaCl. **c**, 1 M NaCl.

https://doi.org/10.1038/s41563-025-02312-9

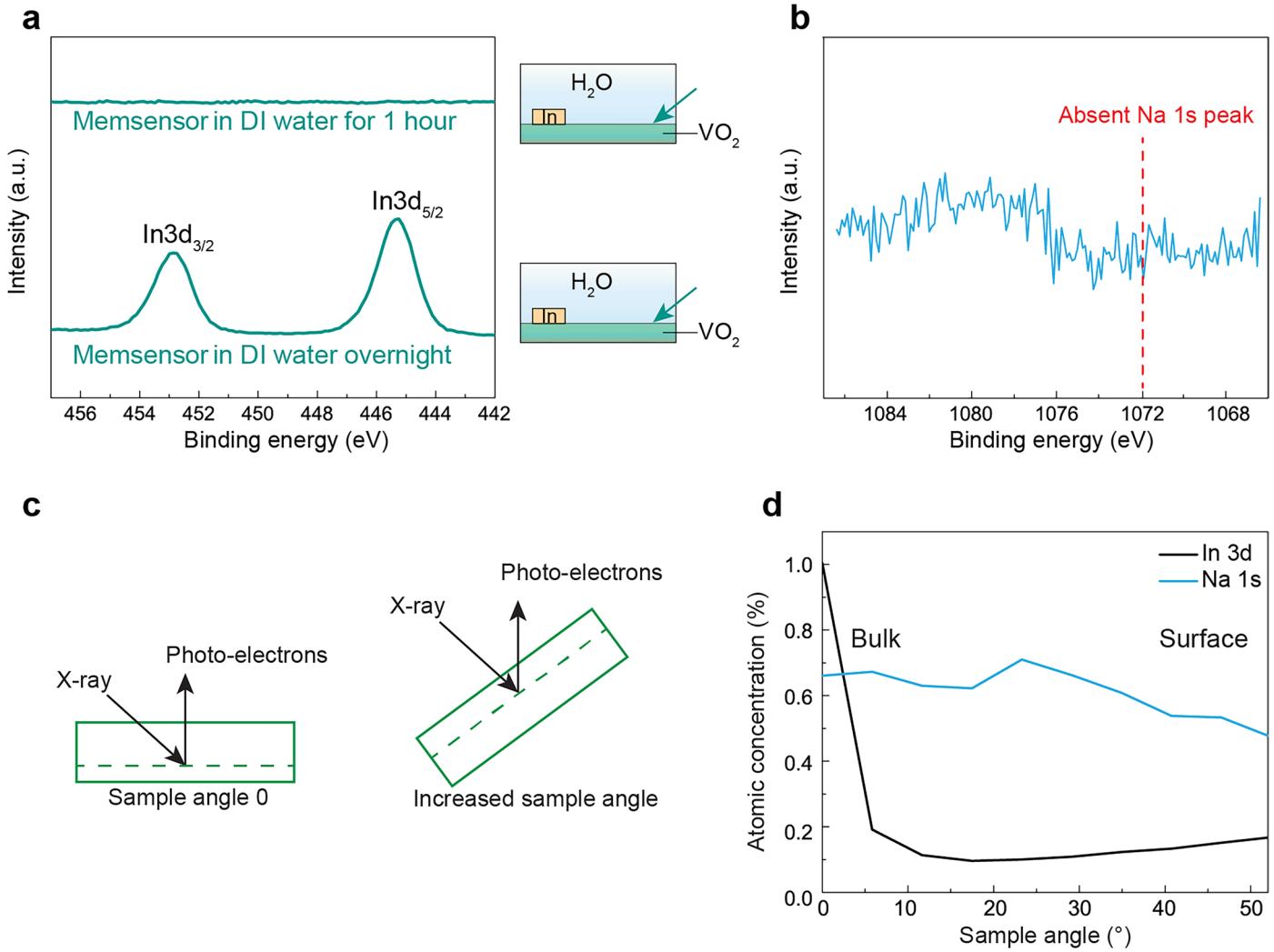


**Extended Data Fig. 5 | Ion doping analysis. a**, Green arrows toward $VO_2$ indicate XPS testing performed on $VO_2$ surface after the sample is removed from water. No indium ion is detected in $VO_2$ after immersing the memsensor in DI water for 1 h (consistent with Fig. 2c). With overnight immersion, indium ions are eventually driven into the $VO_2$ surface. **b**, No Na 1 s peak (~1072 eV) is detected on the $VO_2$ surface in the high-resolution XPS scan after a 5-min treatment of the memsensor in 0.1 M NaCl. **c**, In ARXPS, increased surface sensitivity corresponds to larger sample angles due to reduced penetration depth. **d**, ARXPS analysis of the $VO_2$ surface post-NaCl treatment shows indium within the deeper bulk of $VO_2$, while sodium is localized in the surface area.

https://doi.org/10.1038/s41563-025-02312-9

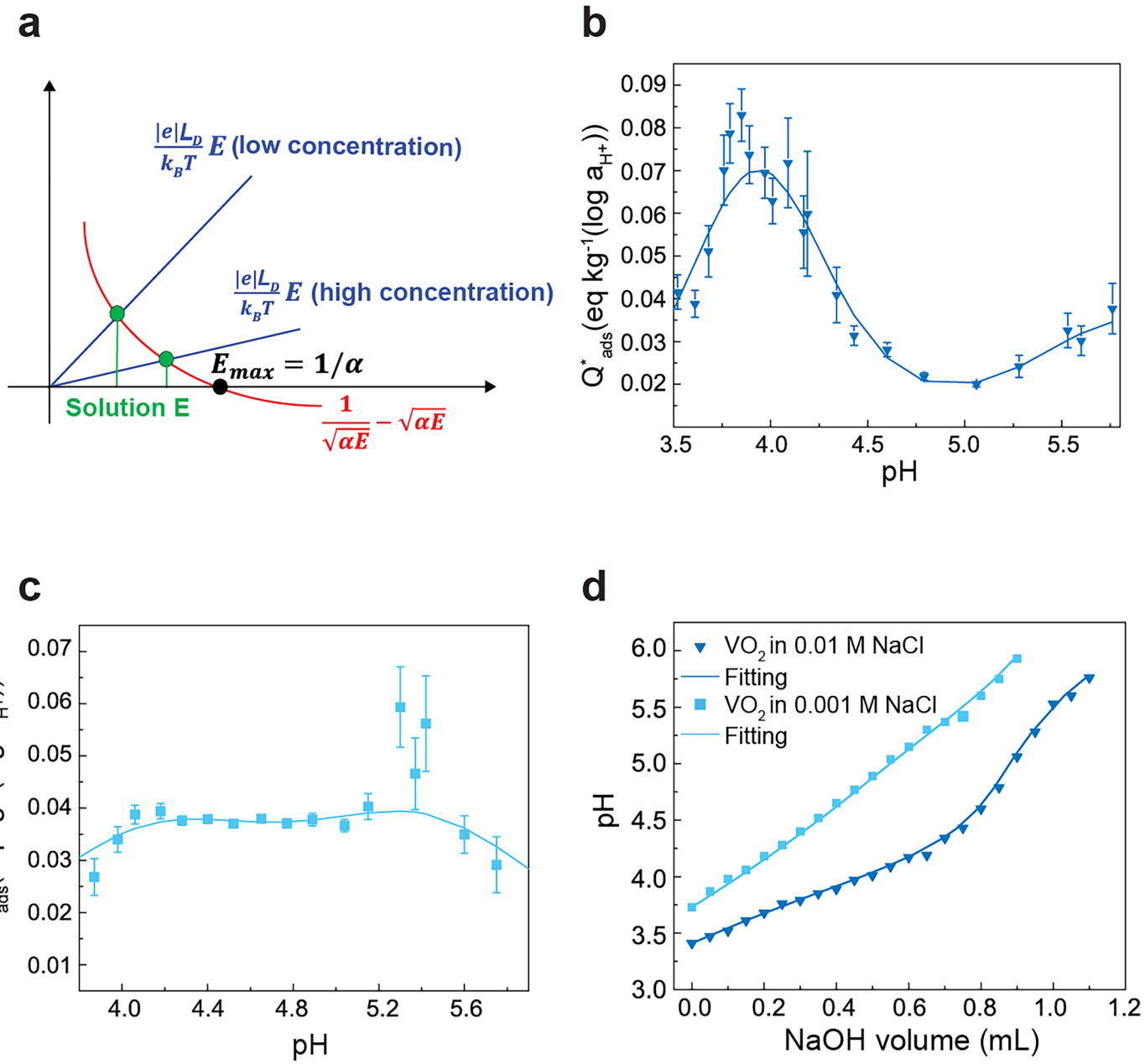


**Extended Data Fig. 6 | Surface electric field analysis. a**, Calculation model to estimate surface electric fields, with electric field strength indicated by the horizontal value at the intersection of the curve and line. **b**–**d**, Fitting titration data to derive the equilibrium constant p$K$, using $Q^*_{ads}$ from titration of 0.01 M NaCl solution (p$K$ = 3.6) (**b**) and 0.001 M NaCl solution (p$K$ = 5.4) (**c**), leading to an automatically fitted titration curve (**d**). $Q_{ads}$ denotes the number of protons exchanged with $VO_2$ powder; $Q^*_{ads}$ is its derivative with respect to pH, estimated using local second-order polynomial regression (that is, a quadratic fit to five neighboring titration points). In (b) and (c), each data point corresponds to a single experimental pH condition (n = 1). Error bars represent the standard deviation of $Q^*_{ads}$ in local fit.

https://doi.org/10.1038/s41563-025-02312-9

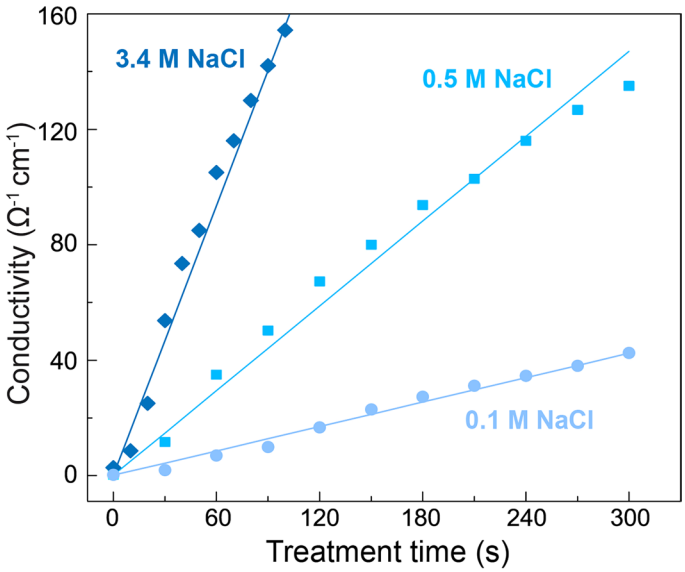


**Extended Data Fig. 7 | Fitting the conductivity data versus treatment time considering both ion diffusion and drift.** The extracted electric fields are summarized in Supplementary Table 2.

https://doi.org/10.1038/s41563-025-02312-9

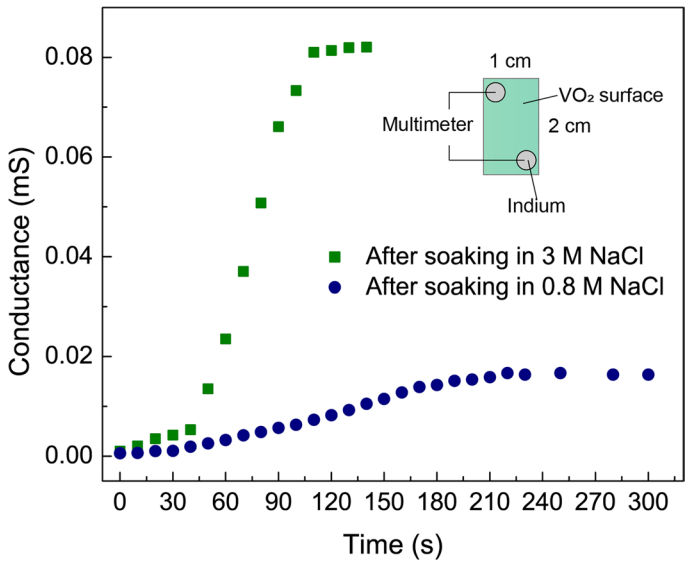


**Extended Data Fig. 8 | Conductance evolution of the memsensor following prolonged treatment with NaCl solutions.** After a brief period of slow increase, the conductance rises linearly, and eventually enters a saturation plateau. For identical memsensor samples (same dimensions, growth batch, etc.), higher NaCl concentrations result in a steeper linear slope and earlier saturation compared to lower concentrations. In this experiment, the samples were identical, and conductance was measured using a multimeter with two indium patches directly serving as electrodes, as illustrated in the inset.

https://doi.org/10.1038/s41563-025-02312-9

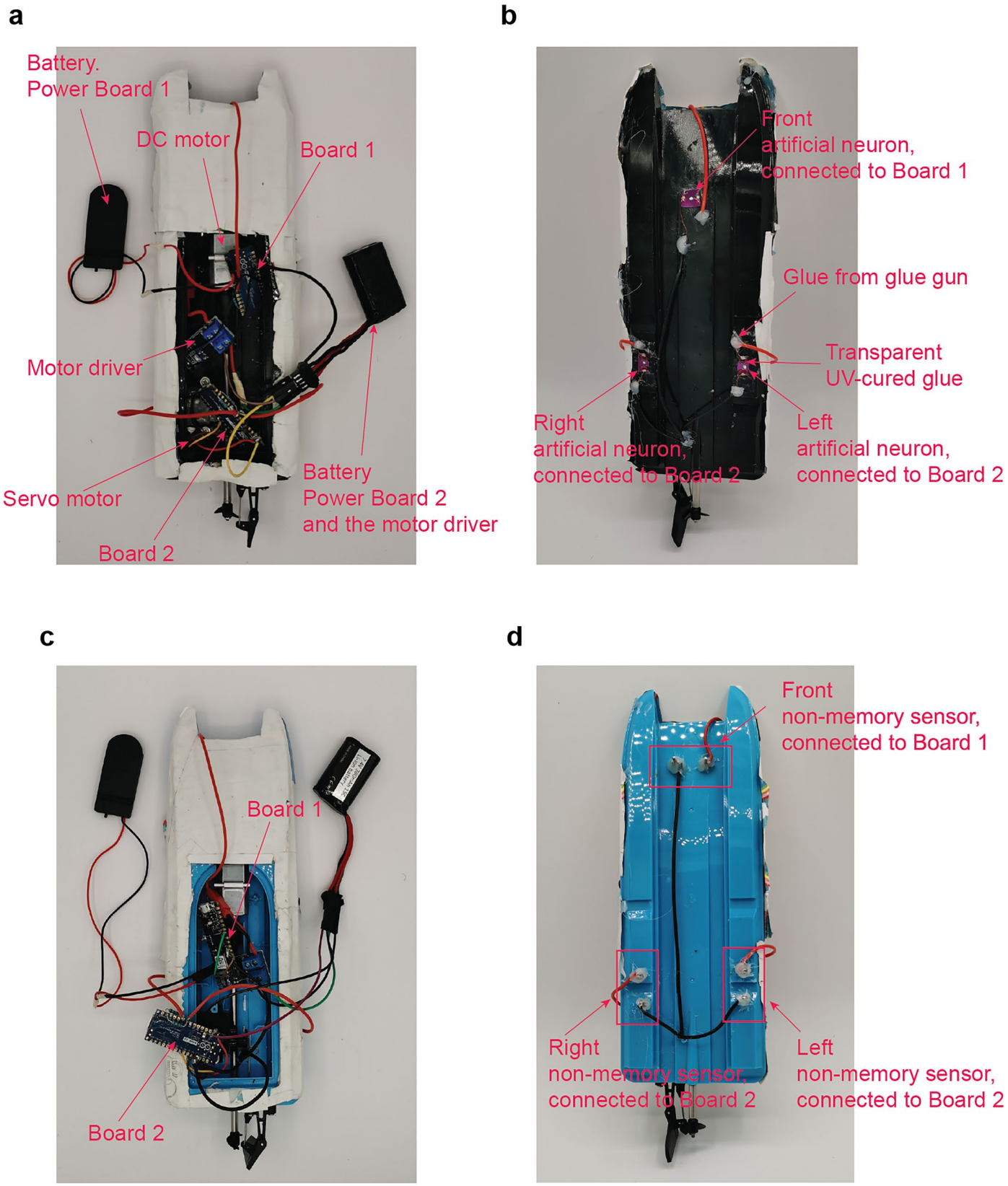


**Extended Data Fig. 9 | Boat design. a**, **b**, Memsensor-equipped boat. (**a**) Board 1 connects to the front sensor and the DC motor, while Board 2 connects to the side sensors and the servo motor. (**b**) Three memsensors are attached to the bottom of the boat. The Right and Left $VO_2$ thin films in are nearly identical. Effects of solution conductance are minimized by sealing wire-$VO_2$ contact points with UV-cured glue and wire connections with hot glue. **c**, **d**, Non-memory sensor-equipped boat. Circuits in (**c**) are similar to that in (**a**), but with fixed resistors of higher resistance (1-2 MΩ) to lower sensor voltage and prevent electrolysis. (**d**) The non-memory sensors are made of two stainless steel electrodes to measure the conductance of the solution.

https://doi.org/10.1038/s41563-025-02312-9

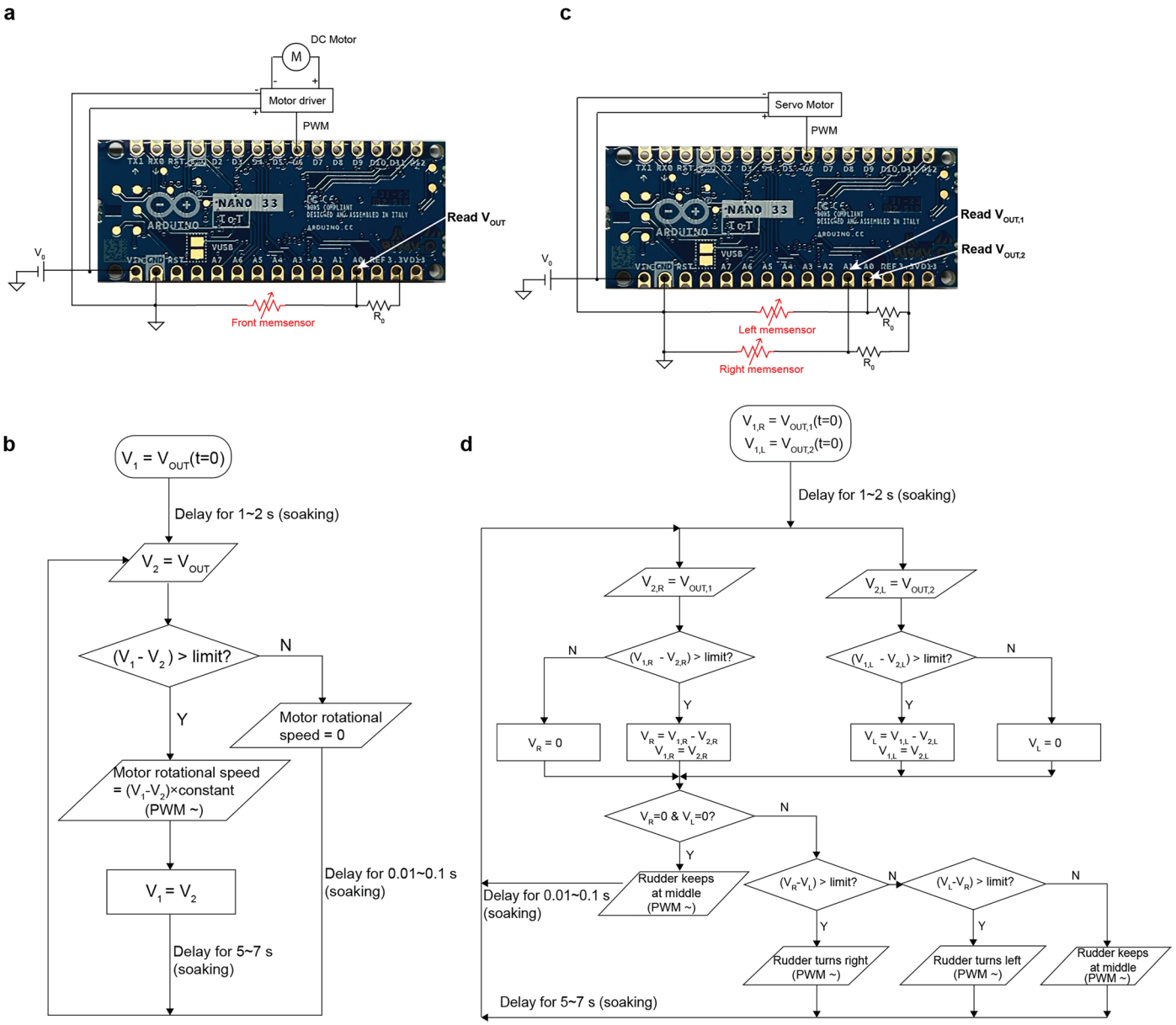


**Extended Data Fig. 10 | Circuits design. a**, **b**, Forward control. $V_{OUT}$ (determined by the Front memsensor's resistance) in Board 1 in (**a**) feeds into algorithm (**b**), controlling the DC motor via pulse width modulation (PWM) signals. (**b**) The algorithm to process the $V_{OUT}$ in (**a**). If the initial voltage difference is minimal, the DC motor remains static, updating $V_2$ after a brief delay. A substantial voltage difference triggers prolonged motor rotation, propelling the boat forward. **c**, **d**, Turning control. $V_{OUT,1}$ and $V_{OUT,2}$ (determined by the Right memsensor and Left memsensor, respectively) in (**c**) are transmitted to the algorithm in (**d**), guiding the PWM signals to control the servo motor. (**d**) The algorithm to process the $V_{OUT,1}$ and $V_{OUT,2}$. Similarly to the process in (**b**), if both the right and left voltage changes are minor, the rudder stays at middle, and $V_{2,R}$ and $V_{2,L}$ are updated quickly. When the voltage difference on either side becomes sufficiently large, the voltage changes are compared for directional changes.